

**Scalable Mach-Zehnder Interferometer  
Optical Switch Chip for Ion-Trap  
Quantum Network**

**Junseo Kwak**

March 2026

Bachelor Thesis  
Keio University

Faculty of Environment and Information Studies

## **Abstract**

Scalable quantum networks require low-loss and reconfigurable photonic interconnects to distribute quantum states between distant nodes. In ion-trap based architectures, visible-wavelength photons at 422 nm are widely used, but integrated optical switching at this wavelength remains challenging compared to the telecom-wavelength. In this thesis, we study a scalable Mach-Zehnder interferometer optical switch chip designed as an elementary  $2 \times 2$  switching unit for ion-trap quantum networks. We design and analyze the chip using a simulation tool named Ansys Lumerical, and we evaluate key performance metrics including loss, extinction ratio, and crosstalk under realistic design constraints. Our results indicate that a compact integrated MZI switch at 422 nm can achieve the switching functionality required for scalable routing, providing a foundation for building larger switching fabrics for quantum networking.

# Contents

<b>1</b>	<b>Introduction</b>	<b>6</b>
1.1	Background and Motivation . . . . .	6
1.2	Photons for Ion-Trap Quantum Networks . . . . .	6
1.3	Native Wavelength Operation and Optical Transducers . . . . .	6
1.4	Scalability and the Role of Switching . . . . .	7
1.5	Integrated Photonics and MZI Switching . . . . .	7
1.6	Challenges at 422 nm . . . . .	7
1.7	Contributions of This Thesis . . . . .	8
1.8	Thesis Structure . . . . .	8
<b>2</b>	<b>Preliminaries</b>	<b>9</b>
2.1	Notations . . . . .	9
2.1.1	Mathematical notation . . . . .	9
2.1.2	Quantum notation . . . . .	9
2.1.3	Photonic operator notation . . . . .	10
2.1.4	Optics notation . . . . .	10
2.1.5	Units and dB . . . . .	10
2.2	Basics of Quantum Information Processing (QIP) . . . . .	11
2.2.1	Qubit and Basis State . . . . .	11
2.2.2	Dirac Notation . . . . .	11
2.2.3	Quantum Superposition . . . . .	11
2.2.4	Unitary Operators . . . . .	12
2.2.5	Bloch Sphere . . . . .	12
2.2.6	Composite Systems and Tensor Products . . . . .	13
2.2.7	Quantum Entanglement . . . . .	14
2.2.8	Bell States . . . . .	14
2.2.9	Mixed States and Density Operators . . . . .	14
2.2.10	Measurement . . . . .	15
2.2.11	Quantum Gates . . . . .	15
2.2.12	Errors, Decoherence, and Fidelity . . . . .	17

2.3	Photonic Encoding and Optical Modes . . . . .	18
2.3.1	Optical Modes . . . . .	18
2.3.2	Single-Photon States and Wavepackets . . . . .	18
2.3.3	Single-Rail and Dual-Rail Encoding . . . . .	19
2.3.4	Polarization Encoding . . . . .	19
2.3.5	Single-Photon Sources . . . . .	20
2.3.6	Time-Bin Encoding . . . . .	20
2.3.7	Relative Phase Between Two Modes . . . . .	20
2.3.8	Conceptual Mapping from Polarization to Time Bin . . . . .	21
2.4	Linear Optical Components . . . . .	21
2.4.1	Two-Mode State Vector . . . . .	21
2.4.2	Two-Mode Mixing Element . . . . .	21
2.4.3	Phase Shifter . . . . .	22
2.4.4	Polarization as a Two-Mode Basis . . . . .	22
2.4.5	Half-Wave Plate . . . . .	22
2.4.6	Polarization Beam Splitter . . . . .	22
2.4.7	Delay Line and Time-Bin Separation . . . . .	22
2.4.8	Polarization to Time-Bin Conversion . . . . .	22
2.5	MZI as an Elementary Switch . . . . .	23
2.5.1	MZI Structure . . . . .	23
2.5.2	MZI Transformation . . . . .	24
2.5.3	Ideal 50:50 Couplers . . . . .	24
2.5.4	Bar and Cross States . . . . .	24
2.5.5	Switching by Phase Control . . . . .	24
2.6	Quantum Network Scalability and the Need for Switching . . . . .	25
2.6.1	Quantum Network View . . . . .	25
2.6.2	Why Switching is Needed . . . . .	25
2.6.3	Elementary $2 \times 2$ Switch . . . . .	25
<b>3</b>	<b>Problem Definition</b>	<b>26</b>
3.1	Scope and Goal . . . . .	26
3.2	System Flow and Interface Assumptions . . . . .	26
3.3	Trapped-Ion Platform . . . . .	26
3.4	Why 422 nm is Not the Telecom Problem . . . . .	27
3.5	Photonic Qubit Constraint . . . . .	27
3.6	Switching Task Definition . . . . .	28
3.7	Loss Budget and Switch Chip Structure . . . . .	28
3.7.1	Loss Budget at 422 nm . . . . .	28

3.7.2	MZI Switch Chip Structure . . . . .	29
3.8	Material Platform and Justification: Lithium Niobate . . . . .	30
3.9	Problem Statement . . . . .	31
<b>4</b>	<b>Method and Design</b>	<b>33</b>
4.1	Ansys Simulation Workflow . . . . .	33
4.1.1	Overview of the Flow . . . . .	33
4.1.2	Common Geometry and Parameter Definition . . . . .	35
4.1.3	MODE FDE Step 1: Optical Modes and Baseline Loss . . . . .	35
4.1.4	CHARGE: Electrostatic Field of the EO Phase Shifter . . . . .	35
4.1.5	MODE FDE Step 2: Pockels Effect and $V_{\pi}L$ Extraction . . . . .	36
4.1.6	EME: Full MZI Propagation and Switching Metrics . . . . .	37
4.1.7	INTERCONNECT Optional: Cascaded Switching Networks . . . . .	38
4.1.8	Summary of Extracted Quantities . . . . .	38
<b>5</b>	<b>Evaluation</b>	<b>39</b>
5.1	MODE . . . . .	39
5.1.1	Material Declaration . . . . .	39
5.1.2	Sellmeier Equation . . . . .	40
5.1.3	Material Declaration in FDE . . . . .	41
5.1.4	Verification Using Material Explorer . . . . .	42
5.1.5	Waveguide Cross-section Geometry in MODE . . . . .	43
5.1.6	Objects and Assigned Materials . . . . .	44
5.1.7	Geometrical Parameters . . . . .	44
5.1.8	FDE Eigenmode Calculation Settings and its Result . . . . .	45
5.2	CHARGE . . . . .	46
5.2.1	Geometry construction in CHARGE . . . . .	46
5.2.2	CHARGE results at 1 V . . . . .	49
5.2.3	$V_{\pi}L$ evaluation by combining CHARGE and MODE results . . . . .	52
5.2.4	Final $V_{\pi}L$ results and comparison . . . . .	54
<b>6</b>	<b>Conclusion</b>	<b>56</b>

# List of Figures

2.1	Bloch sphere representation of a single-qubit state . . . . .	13
2.2	Pauli $X$ Gate in a quantum circuit . . . . .	15
2.3	Pauli $Y$ Gate in a quantum circuit . . . . .	16
2.4	Pauli $Z$ Gate in a quantum circuit . . . . .	16
2.5	$H$ Gate in a quantum circuit . . . . .	16
2.6	CNOT Gate in a quantum circuit . . . . .	17
2.7	Experiment set-up of conversion from [1] . . . . .	23
2.8	Mach-Zehnder interferometer structure for two path modes . . . . .	23
5.1	Reference dispersion of $\text{LiNbO}_3$ ordinary refractive index $n_o(\lambda)$ . At $\lambda = 0.422 \mu\text{m}$ , $n_o = 2.4089$ . . . . .	40
5.2	Reference dispersion of $\text{LiNbO}_3$ extraordinary refractive index $n_e(\lambda)$ . At $\lambda = 0.422 \mu\text{m}$ , $n_e = 2.3063$ . . . . .	40
5.3	Custom material declaration in Lumerical for $\text{LiNbO}_3\_x\text{cut\_}20\text{C}$ using a diagonal anisotropic Sellmeier model. Coefficients for $xx$ and $yy$ correspond to $n_o(\lambda)$ , and those for $zz$ correspond to $n_e(\lambda)$ . . . . .	41
5.4	Material explorer check for the declared $\text{LiNbO}_3\_x\text{cut\_}20\text{C}$ material: ordinary-index component ( $xx/yy$ ). The value at $\lambda \approx 0.422 \mu\text{m}$ matches $n_o \simeq 2.4089$ . . . . .	42
5.5	Material explorer check for the declared $\text{LiNbO}_3\_x\text{cut\_}20\text{C}$ material: extraordinary-index component ( $zz$ ). The value at $\lambda \approx 0.422 \mu\text{m}$ matches $n_e \simeq 2.3063$ . . . . .	43
5.6	Geometry objects and material assignments in MODE. . . . .	44
5.7	MODE calculation settings and field plot at $\lambda = 0.422 \mu\text{m}$ . The displayed plot shows the electric-field intensity ( $ E ^2$ ) distribution in the $x-y$ cross-section. . . . .	45
5.8	CHARGE geometry construction and object trees used for the electrostatic simulation. . . . .	47

5.9	CHARGE result: $E_x(x, y)$ distribution under a single-ended 1 V drive ( $V_{\text{sig}} = 1$ V, $V_{\text{gnd}} = 0$ V). The field is concentrated near electrode edges and across the electrode gap, with a finite penetration into the LN waveguide region. . . . .	50
5.10	CHARGE result: $E_y(x, y)$ distribution under a single-ended 1 V drive. This component is later mapped to the LN $c$ -axis field component $E_c$ according to the adopted crystal-axis mapping and is used to evaluate the EO overlap with the optical TE <sub>0</sub> mode. . . . .	51
5.11	CHARGE result: electrostatic potential $V(x, y)$ for a 1 V single-ended bias. The potential drop is localized around the electrode gap region, validating the applied boundary conditions and the simulation region coverage. . . . .	51

## List of Tables

2.1	Six cardinal states on the Bloch sphere . . . . .	13
3.1	Comparison of integrated photonics material platforms . . . . .	31
4.1	Overview flow of simulation . . . . .	34
5.1	Geometry objects and material assignments in MODE . . . . .	44

# Chapter 1

## Introduction

### 1.1 Background and Motivation

Quantum networks aim to connect spatially separated quantum nodes and enable the distribution of quantum states over long distances. Photons are natural carriers of quantum information because they propagate through free space and optical fibers while preserving coherence over distance.

For long-distance transmission, the telecom band near 1550 nm is widely used due to low fiber attenuation. At the same time, many quantum emitters generate photons at visible or near-visible wavelengths. This wavelength mismatch motivates two complementary directions: direct photonic processing at the native emission wavelength and wavelength interfacing to telecom links.

### 1.2 Photons for Ion-Trap Quantum Networks

Trapped-ion platforms use optical photons to interface stationary qubits with flying photonic qubits. The relevant photon wavelength is species-dependent and set by the ion optical transitions. In this thesis, we focus on the  $^{88}\text{Sr}^+$  platform, where an important transition is around 422 nm. Photons near 422 nm are used in quantum networking primitives such as remote entanglement generation and state transfer.

### 1.3 Native Wavelength Operation and Optical Transducers

One approach to long-distance networking is to convert visible photons to the telecom band using optical transducers such as quantum frequency conversion. This approach

is actively studied and can enable low-loss fiber transmission. However, transduction introduces additional optical components and constraints, and overall system performance depends on conversion efficiency, added noise, and total insertion loss.

For this reason, it is also valuable to study direct photonic processing at the native emission wavelength of the quantum source. In particular, integrated switching at 422 nm can serve as a building block for routing and multiplexing in Sr<sup>+</sup>-based architectures.

## 1.4 Scalability and the Role of Switching

A central challenge in scaling a quantum network is routing. As the number of nodes and links grows, fixed point-to-point optical layouts become inefficient because they require dedicated hardware for each connection pattern. Reconfigurable optical switching addresses this limitation by enabling dynamic path selection and resource sharing. A compact and repeatable  $2 \times 2$  switching element is especially important because large switching fabrics can be built by elementary blocks.

## 1.5 Integrated Photonics and MZI Switching

Integrated photonics provides an attractive route to scalable switching. Compared to bulk optical implementations, integrated devices offer improved phase stability, reduced alignment complexity, and a compact footprint suitable for large-scale integration. Among various switching structures, the Mach-Zehnder interferometer is a standard choice because it implements switching through controllable interference between two arms. By adjusting the relative phase between the arms, an MZI can realize the bar and cross states of a  $2 \times 2$  switch.

## 1.6 Challenges at 422 nm

Integrated MZI switching has been extensively demonstrated at telecom wavelengths near 1550 nm. Extending high-performance operation to visible wavelengths such as 422 nm introduces additional constraints. Propagation loss and scattering from sidewall roughness can become more severe at shorter wavelengths. Fabrication tolerances also tighten because dimensional variations can induce larger effective-index changes and phase imbalance. These effects reduce switching contrast and increase crosstalk unless the device design is carefully optimized.

## 1.7 Contributions of This Thesis

This thesis focuses on the design and evaluation of a scalable Mach-Zehnder interferometer optical switch chip for ion-trap quantum networking at 422 nm. We use Ansys Lumerical to model the optical behavior and quantify performance metrics relevant to switching networks. The main contributions are summarized as follows.

- We define switching requirements motivated by scalable ion-trap quantum networking at 422 nm.
- We propose an MZI-based  $2 \times 2$  switch design and a simulation methodology for evaluating its behavior.
- We report switching performance metrics and discuss the implications for scalable network architectures.

## 1.8 Thesis Structure

The remainder of this thesis is organized as follows. Chapter 2 introduces background concepts in quantum information processing and photonic encodings, and it establishes the linear-optics formalism used throughout the design. Chapter 3 defines the switching problem at 422 nm and specifies target performance requirements. Chapter 4 presents the proposed MZI switch design and simulation methodology. Chapter 5 evaluates the switching performance and discusses the implications for scalable quantum network architectures. Finally, Chapter 6 concludes the thesis and outlines future directions.

# Chapter 2

## Preliminaries

### 2.1 Notations

This section summarizes the notations used throughout this thesis.

#### 2.1.1 Mathematical notation

- $\mathbb{R}$  : real numbers
- $\mathbb{C}$  : complex numbers
- $i$  : imaginary unit,  $i^2 = -1$
- $(\cdot)^*$  : complex conjugate
- $(\cdot)^\dagger$  : Hermitian adjoint
- $\mathbf{I}$  : identity operator
- $\text{Tr}(\cdot)$  : trace
- $[A, B]$  : commutator,  $[A, B] = AB - BA$
- $\otimes$  : tensor product

#### 2.1.2 Quantum notation

- $\mathcal{H}$  : Hilbert space
- $|\psi\rangle$  : ket
- $\langle\phi|$  : bra

- $\langle \phi | \psi \rangle$  : inner product
- $|\psi\rangle\langle\phi|$  : outer product operator
- $\rho$  : density operator
- $F(\rho, \sigma)$  : state fidelity

### 2.1.3 Photonic operator notation

- $a$  : annihilation operator of an optical mode
- $a^\dagger$  : creation operator of an optical mode
- $|n\rangle$  : Fock state with photon number  $n$
- $a^\dagger a$  : photon-number operator
- $[a, a^\dagger] = 1$  : bosonic commutation relation

### 2.1.4 Optics notation

- $\lambda$  : wavelength in vacuum
- $f$  : frequency
- $\omega$  : angular frequency
- $k_0$  : vacuum wavenumber
- $c$  : speed of light in vacuum
- $\omega = 2\pi f$
- $f = c/\lambda$
- $k_0 = 2\pi/\lambda$

### 2.1.5 Units and dB

- nm : nanometer
- $\mu\text{m}$  : micrometer
- dB power ratio

$$P_{\text{dB}} = 10 \log_{10} \left( \frac{P}{P_0} \right)$$

## 2.2 Basics of Quantum Information Processing (QIP)

### 2.2.1 Qubit and Basis State

A qubit is the fundamental unit of quantum information. The computational basis states are

$$|0\rangle = \begin{pmatrix} 1 \\ 0 \end{pmatrix}, \quad |1\rangle = \begin{pmatrix} 0 \\ 1 \end{pmatrix}. \quad (2.1)$$

A pure state of a qubit is written as

$$|\psi\rangle = \alpha|0\rangle + \beta|1\rangle, \quad |\alpha|^2 + |\beta|^2 = 1, \quad (2.2)$$

where  $\alpha, \beta \in \mathbb{C}$  are probability amplitudes. Measurement in the computational basis returns the outcome  $|0\rangle$  with probability  $|\alpha|^2$  and  $|1\rangle$  with probability  $|\beta|^2$ . The amplitudes are complex numbers, so the relative phase between  $\alpha$  and  $\beta$  can affect interference phenomena.

### 2.2.2 Dirac Notation

Dirac notation provides a compact representation of quantum states and linear operators. A state vector is written as a ket  $|\psi\rangle$ , and its Hermitian adjoint is written as a bra  $\langle\psi|$ . The inner product is a complex number

$$\langle\phi|\psi\rangle \in \mathbb{C}, \quad (2.3)$$

and it describes how similar two states are. If  $\langle\phi|\psi\rangle = 0$ , the two states are orthogonal. The outer product

$$|\psi\rangle\langle\phi| \quad (2.4)$$

represents a linear operator. A common example is the projector  $|\psi\rangle\langle\psi|$ , which selects the component of a state along  $|\psi\rangle$ .

### 2.2.3 Quantum Superposition

Superposition means that a linear combination of valid states is also a valid quantum state. In an  $n$ -dimensional Hilbert space with an orthonormal basis  $|n\rangle$ , any pure state can be written as

$$|\psi\rangle = \sum_n a_n |n\rangle, \quad (2.5)$$

where  $a_n$  are probability amplitudes.

Superposition is often contrasted with classical randomness. In a classical mixture, one would say the system is either  $|0\rangle$  or  $|1\rangle$  with some probability. In a superposition, both components coexist at the level of amplitudes, and this can produce interference.

A well-known physical example is the double-slit experiment. When a single particle passes through a pair of slits, the detection pattern on a screen shows interference fringes. This behavior is explained by treating the state as a superposition of two path alternatives, rather than a classical choice of one path.

### 2.2.4 Unitary Operators

A linear operator  $U : \mathcal{H} \rightarrow \mathcal{H}$  is called unitary if

$$U^\dagger U = UU^\dagger = I. \quad (2.6)$$

A unitary transformation preserves inner products and therefore preserves normalization. In quantum information processing, unitary operators represent reversible evolutions and gate operations. When applied to a state vector,

$$|\psi'\rangle = U|\psi\rangle. \quad (2.7)$$

### 2.2.5 Bloch Sphere

The Bloch sphere is a geometric representation of a pure single-qubit state. Any pure state satisfying Eq.(2.2) can be parametrized by angles  $\theta$  and  $\phi$ :

$$|\psi\rangle = \cos\left(\frac{\theta}{2}\right)|0\rangle + e^{i\phi} \sin\left(\frac{\theta}{2}\right)|1\rangle, \quad \theta \in [0, \pi], \quad \phi \in [0, 2\pi). \quad (2.8)$$

The angle  $\theta$  determines the relative weights of  $|0\rangle$  and  $|1\rangle$ . The angle  $\phi$  determines the relative phase between them.

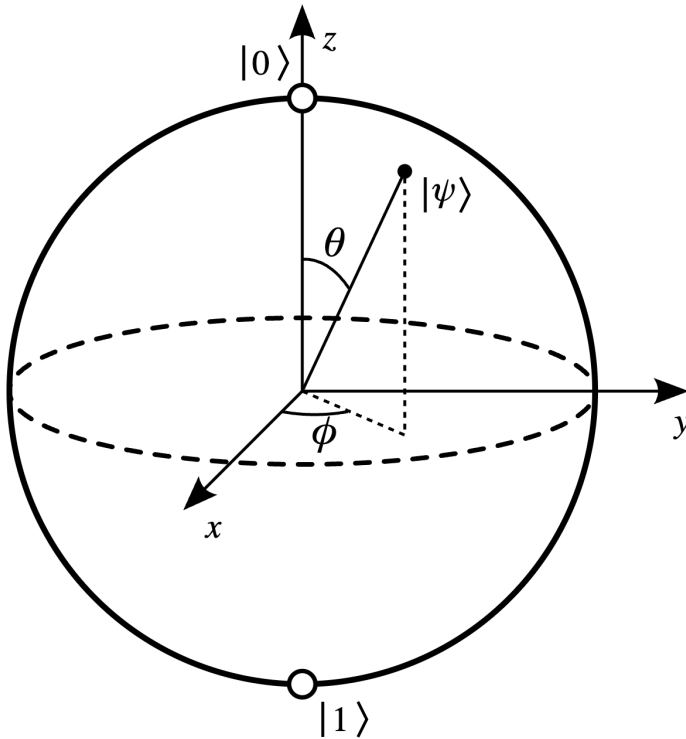


Figure 2.1: Bloch sphere representation of a single-qubit state

The six cardinal states correspond to specific values of  $\theta$  and  $\phi$ :

State	$(\theta, \phi)$	$ \psi\rangle$
+Z	$(0, 0)$	$ 0\rangle$
-Z	$(\pi, 0)$	$ 1\rangle$
+X	$(\frac{\pi}{2}, 0)$	$\frac{1}{\sqrt{2}}( 0\rangle +  1\rangle)$
-X	$(\frac{\pi}{2}, \pi)$	$\frac{1}{\sqrt{2}}( 0\rangle -  1\rangle)$
+Y	$(\frac{\pi}{2}, \frac{\pi}{2})$	$\frac{1}{\sqrt{2}}( 0\rangle + i 1\rangle)$
-Y	$(\frac{\pi}{2}, \frac{3\pi}{2})$	$\frac{1}{\sqrt{2}}( 0\rangle - i 1\rangle)$

Table 2.1: Six cardinal states on the Bloch sphere

## 2.2.6 Composite Systems and Tensor Products

For two quantum systems  $A$  and  $B$ , the joint Hilbert space is  $\mathcal{H}_A \otimes \mathcal{H}_B$ . If  $|\psi\rangle_A$  and  $|\phi\rangle_B$  are states of each subsystem, a product state is written as

$$|\psi\rangle_A \otimes |\phi\rangle_B. \quad (2.9)$$

This notation is used to describe multi-qubit systems and correlations between subsystems.

### 2.2.7 Quantum Entanglement

For two quantum systems  $A$  and  $B$ , a general joint state can be written as

$$|\psi\rangle = \sum_{i,j} C_{ij} |i\rangle_A \otimes |j\rangle_B. \quad (2.10)$$

If the state cannot be written as  $|\psi\rangle_A \otimes |\phi\rangle_B$ , it is entangled. Entanglement is a form of correlation that cannot be reproduced by assigning independent states to the two subsystems.

### 2.2.8 Bell States

Continuing with a two-qubit system, the four maximally entangled Bell states are

$$|\Phi^\pm\rangle = \frac{1}{\sqrt{2}}(|00\rangle \pm |11\rangle), \quad |\Psi^\pm\rangle = \frac{1}{\sqrt{2}}(|01\rangle \pm |10\rangle). \quad (2.11)$$

These states are frequently used as standard reference states when discussing entanglement and correlations.

### 2.2.9 Mixed States and Density Operators

A mixed state is a probabilistic mixture of pure states  $|\psi_i\rangle$  occurring with probabilities  $p_i$ . It is represented by the density operator

$$\rho = \sum_i p_i |\psi_i\rangle\langle\psi_i|, \quad p_i \geq 0, \quad \sum_i p_i = 1. \quad (2.12)$$

The density operator satisfies

$$\rho = \rho^\dagger, \quad \rho \succeq 0, \quad \text{Tr } \rho = 1. \quad (2.13)$$

A pure state  $|\psi\rangle$  corresponds to  $\rho = |\psi\rangle\langle\psi|$ . For a bipartite state  $\rho_{AB}$ , the reduced state of subsystem  $A$  is obtained by the partial trace

$$\rho_A = \text{Tr}_B(\rho_{AB}). \quad (2.14)$$

### 2.2.10 Measurement

Measurement maps a quantum state to a classical outcome. We describe a projective measurement using projectors  $\{\Pi_m\}$  that satisfy

$$\Pi_m = \Pi_m^\dagger, \quad \Pi_m^2 = \Pi_m, \quad \sum_m \Pi_m = \mathbf{I}. \quad (2.15)$$

For a pure state  $|\psi\rangle$ , the probability of outcome  $m$  is

$$p(m) = \langle \psi | \Pi_m | \psi \rangle. \quad (2.16)$$

For a mixed state  $\rho$ , the probability is

$$p(m) = \text{Tr}(\Pi_m \rho). \quad (2.17)$$

After obtaining outcome  $m$ , the post-measurement state becomes

$$\rho' = \frac{\Pi_m \rho \Pi_m}{\text{Tr}(\Pi_m \rho)}. \quad (2.18)$$

### 2.2.11 Quantum Gates

Like classical logic gates, we can apply a quantum gate onto qubits to manipulate their states. The most common single and two-qubit gates are:

#### Pauli $X$ Gate

$$X = \sigma_x = \begin{pmatrix} 0 & 1 \\ 1 & 0 \end{pmatrix} \quad (2.19)$$

When we apply Pauli  $X$  gate onto a qubit state  $|0\rangle$ , it swaps its state to  $|1\rangle$  and vice versa. It acts as a *NOT* gate in classical circuits.

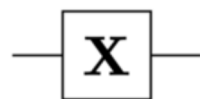


Figure 2.2: Pauli  $X$  Gate in a quantum circuit

**Pauli  $Y$  Gate**

$$Y = \sigma_y = \begin{pmatrix} 0 & -i \\ i & 0 \end{pmatrix} \quad (2.20)$$

The Pauli  $Y$  gate combines a bit-flip with a phase shift.

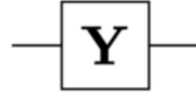


Figure 2.3: Pauli  $Y$  Gate in a quantum circuit

**Pauli  $Z$  Gate**

$$Z = \sigma_z = \begin{pmatrix} 1 & 0 \\ 0 & -1 \end{pmatrix} \quad (2.21)$$

The Pauli  $Z$  gate flips the phase of  $|1\rangle$  relative to  $|0\rangle$ .

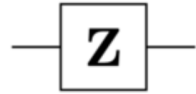


Figure 2.4: Pauli  $Z$  Gate in a quantum circuit

**Hadamard Gate**

$$H = \frac{1}{\sqrt{2}} \begin{pmatrix} 1 & 1 \\ 1 & -1 \end{pmatrix} \quad (2.22)$$

The Hadamard gate maps computational basis states to equal superpositions.

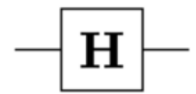


Figure 2.5:  $H$  Gate in a quantum circuit

### Controlled NOT (CNOT) Gate

$$\text{CNOT} = \begin{pmatrix} 1 & 0 & 0 & 0 \\ 0 & 1 & 0 & 0 \\ 0 & 0 & 0 & 1 \\ 0 & 0 & 1 & 0 \end{pmatrix} \quad (2.23)$$

The CNOT gate acts on two qubits, a control and a target.

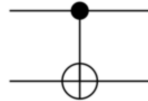


Figure 2.6: CNOT Gate in a quantum circuit

### 2.2.12 Errors, Decoherence, and Fidelity

In practice, the implemented quantum state deviates from the ideal target state due to noise and decoherence. Noise and decoherence can be modeled by a quantum channel  $\mathcal{E}$  that maps density operators to density operators. A general representation uses Kraus operators  $\{E_k\}$ :

$$\mathcal{E}(\rho) = \sum_k E_k \rho E_k^\dagger, \quad \sum_k E_k^\dagger E_k = \mathbf{I}. \quad (2.24)$$

#### Pauli Error Channels

A convenient model for errors on a single qubit uses Pauli operators

$$X = \begin{pmatrix} 0 & 1 \\ 1 & 0 \end{pmatrix}, \quad Z = \begin{pmatrix} 1 & 0 \\ 0 & -1 \end{pmatrix}, \quad Y = iXZ. \quad (2.25)$$

A bit-flip error is modeled by applying  $X$ . A phase-flip error is modeled by applying  $Z$ . A general Pauli error model is expressed as a probabilistic mixture of Pauli operations acting on the density operator  $\rho$

$$\mathcal{E}_{\text{Pauli}}(\rho) = p_I \rho + p_X X \rho X + p_Y Y \rho Y + p_Z Z \rho Z, \quad p_I + p_X + p_Y + p_Z = 1. \quad (2.26)$$

#### Amplitude Damping

Amplitude damping models relaxation from  $|1\rangle$  to  $|0\rangle$ . It is described by Kraus operators

$$E_0 = \begin{pmatrix} 1 & 0 \\ 0 & \sqrt{1-\gamma} \end{pmatrix}, \quad E_1 = \begin{pmatrix} 0 & \sqrt{\gamma} \\ 0 & 0 \end{pmatrix}, \quad (2.27)$$

and the channel acts as

$$\mathcal{E}_{\text{AD}}(\rho) = E_0 \rho E_0^\dagger + E_1 \rho E_1^\dagger. \quad (2.28)$$

The parameter  $\gamma$  quantifies the relaxation strength.

### State Fidelity

We use fidelity to quantify how close a realized state  $\rho$  is to a target state  $\sigma$ . The general definition is

$$F(\rho, \sigma) = \left( \text{Tr} \sqrt{\sqrt{\rho} \sigma \sqrt{\rho}} \right)^2. \quad (2.29)$$

For a pure target state  $\sigma = |\psi\rangle\langle\psi|$ , fidelity reduces to

$$F(\rho, |\psi\rangle) = \langle\psi|\rho|\psi\rangle. \quad (2.30)$$

A larger fidelity indicates a higher-quality implementation of the desired state.

## 2.3 Photonic Encoding and Optical Modes

### 2.3.1 Optical Modes

An optical mode is a distinguishable degree of freedom of light used to carry information. Typical examples are spatial path, polarization, time, and frequency.

### 2.3.2 Single-Photon States and Wavepackets

A single photon in one optical mode is described in the Fock basis. We denote the vacuum state by  $|\text{vac}\rangle$  and the single-photon state by  $|1\rangle$ . Using the creation operator  $a^\dagger$ , we write

$$|1\rangle = a^\dagger |\text{vac}\rangle. \quad (2.31)$$

A realistic single photon occupies a wavepacket with a finite bandwidth. We describe a single-photon wavepacket by a normalized spectral amplitude function  $\xi(\omega)$  such that

$$\int |\xi(\omega)|^2 d\omega = 1. \quad (2.32)$$

The central wavelength  $\lambda$  is related to the central angular frequency  $\omega_0$  by

$$\omega_0 = \frac{2\pi c}{\lambda}. \quad (2.33)$$

The linewidth  $\Delta\omega$  determines the coherence time scale

$$\tau_c \sim \frac{1}{\Delta\omega}, \quad (2.34)$$

and the coherence length scale

$$L_c = c \tau_c. \quad (2.35)$$

In time-bin encoding, two temporal components must remain phase-coherent. We choose the time-bin separation  $\tau$  with respect to the coherence time scale.

### 2.3.3 Single-Rail and Dual-Rail Encoding

Photonic qubits can be encoded using single-rail or dual-rail schemes.

#### Single-Rail Encoding

Single-rail encoding uses the vacuum and single-photon Fock states of one mode:

$$|0\rangle \equiv |\text{vac}\rangle, \quad |1\rangle \equiv |1\rangle. \quad (2.36)$$

This encoding is conceptually simple but requires distinguishing vacuum from loss.

#### Dual-Rail Encoding

Dual-rail encoding uses two distinct path modes, labeled  $a$  and  $b$ , with exactly one photon shared between them:

$$|0\rangle \equiv |1\rangle_a |0\rangle_b, \quad |1\rangle \equiv |0\rangle_a |1\rangle_b. \quad (2.37)$$

A general dual-rail qubit state is written as

$$|\psi\rangle = \alpha|1\rangle_a |0\rangle_b + \beta|0\rangle_a |1\rangle_b, \quad |\alpha|^2 + |\beta|^2 = 1. \quad (2.38)$$

In integrated photonics, dual-rail encoding naturally maps to two waveguides.

### 2.3.4 Polarization Encoding

Polarization encoding uses two orthogonal polarization modes, horizontal and vertical, as a qubit basis. We define

$$|0\rangle \equiv |H\rangle, \quad |1\rangle \equiv |V\rangle. \quad (2.39)$$

A general polarization qubit state is

$$|\psi\rangle = \alpha|H\rangle + \beta|V\rangle, \quad |\alpha|^2 + |\beta|^2 = 1. \quad (2.40)$$

Polarization encoding is widely used because it is easy to prepare and analyze using standard optical elements.

### 2.3.5 Single-Photon Sources

Single photons can be produced by heralding from photon-pair generation. A widely used process is spontaneous parametric down-conversion also known as SPDC. A pump laser drives a nonlinear medium, typically Lithium Niobate, and probabilistically generates a signal photon and an idler photon. Detecting the idler photon heralds the presence of the signal photon.

The same process can generate entangled photon pairs. These pairs are a standard resource for distributing entanglement across a quantum network.

### 2.3.6 Time-Bin Encoding

Time-bin encoding uses two separated arrival times as a qubit basis. We define

$$|0\rangle \equiv |e\rangle, \quad |1\rangle \equiv |l\rangle, \quad (2.41)$$

where  $|e\rangle$  denotes the early time bin and  $|l\rangle$  denotes the late time bin. A general time-bin qubit state is

$$|\psi\rangle = \alpha|e\rangle + \beta|l\rangle, \quad |\alpha|^2 + |\beta|^2 = 1. \quad (2.42)$$

The separation between the two time bins is denoted by  $\tau$ . Time-bin encoding is well suited for fiber transmission because polarization fluctuations in the channel do not directly mix the two temporal modes.

### 2.3.7 Relative Phase Between Two Modes

Interference depends on the relative phase between two coherent contributions. We represent a relative phase shift  $\phi$  in a two-mode basis by

$$\alpha|0\rangle + \beta|1\rangle \longrightarrow \alpha|0\rangle + e^{i\phi}\beta|1\rangle. \quad (2.43)$$

The relative phase  $\phi$  is observable through interference, while a global phase is not observable.

### 2.3.8 Conceptual Mapping from Polarization to Time Bin

We conceptually map polarization basis states into temporal basis states. Under an ideal mapping, we use

$$|H\rangle \longrightarrow |e\rangle, \quad |V\rangle \longrightarrow e^{i\phi}|l\rangle, \quad (2.44)$$

so that

$$\alpha|H\rangle + \beta|V\rangle \longrightarrow \alpha|e\rangle + e^{i\phi}\beta|l\rangle. \quad (2.45)$$

This mapping preserves the qubit amplitudes and transfers the logical basis from polarization to arrival time. We describe the optical components used for this conversion in the next section.

## 2.4 Linear Optical Components

### 2.4.1 Two-Mode State Vector

We represent the complex mode amplitudes as a column vector

$$\mathbf{a} = \begin{pmatrix} a_1 \\ a_2 \end{pmatrix}. \quad (2.46)$$

In this section, we assume an ideal lossless component, so the transformation is unitary and preserves total power.

$$\mathbf{a}_{\text{out}} = U \mathbf{a}_{\text{in}}, \quad U^\dagger U = I. \quad (2.47)$$

### 2.4.2 Two-Mode Mixing Element

A two-mode mixing element redistributes amplitudes between two modes. We model this element by a unitary matrix  $U_C(\kappa)$

$$U_C(\kappa) = \begin{pmatrix} \cos \kappa & i \sin \kappa \\ i \sin \kappa & \cos \kappa \end{pmatrix}. \quad (2.48)$$

The corresponding power splitting ratio is  $\cos^2 \kappa : \sin^2 \kappa$ . The case  $\kappa = \pi/4$  gives a 50 : 50 mixing.

### 2.4.3 Phase Shifter

A phase shifter applies a relative phase between two modes. A phase shift on the second mode is written as

$$U_\phi = \begin{pmatrix} 1 & 0 \\ 0 & e^{i\phi} \end{pmatrix}. \quad (2.49)$$

### 2.4.4 Polarization as a Two-Mode Basis

In polarization encoding, the two-mode basis is  $|H\rangle$  and  $|V\rangle$ . We represent the polarization amplitudes by

$$\mathbf{a}_{\text{pol}} = \begin{pmatrix} a_H \\ a_V \end{pmatrix}. \quad (2.50)$$

### 2.4.5 Half-Wave Plate

A half-wave plate applies a unitary transformation in the polarization basis. For a rotation angle  $\theta$ , we use

$$U_{\text{HWP}}(\theta) = \begin{pmatrix} \cos 2\theta & \sin 2\theta \\ \sin 2\theta & -\cos 2\theta \end{pmatrix}. \quad (2.51)$$

### 2.4.6 Polarization Beam Splitter

A polarization beam splitter separates  $|H\rangle$  and  $|V\rangle$  into different spatial paths. PBS can route two polarization components into two arms of an interferometer.

### 2.4.7 Delay Line and Time-Bin Separation

A delay line introduces a time shift  $\tau$  between two arms. This delay defines the separation between the early and late time bins after recombination.

### 2.4.8 Polarization to Time-Bin Conversion

Conversion from polarization encoding into time-bin encoding is possible using optical components such as PBS, HWP, and beam splitter. The PBS separates  $|H\rangle$  and  $|V\rangle$  into two arms. Place a delay line in one arm to introduce  $\tau$ . Apply an HWP so that both arms have the same polarization before recombination. Then, recombine the two arms using a beam splitter. After recombination, the information is carried by time bins. Conversion at the state level can be described by

$$\alpha|H\rangle + \beta|V\rangle \longrightarrow \alpha|e\rangle + e^{i\phi}\beta|l\rangle, \quad (2.52)$$

where  $\phi$  is the controllable relative phase between the two arms.

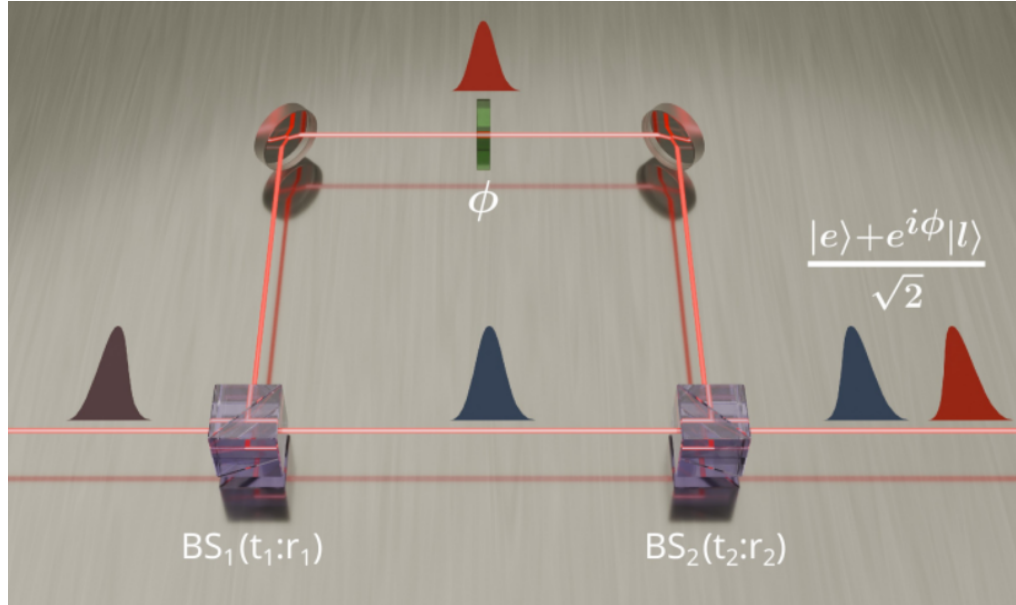


Figure 2.7: Experiment set-up of conversion from [1]

## 2.5 MZI as an Elementary Switch

### 2.5.1 MZI Structure

A Mach-Zehnder Interferometer consists of two couplers and two arms that accumulate different phases. We model the MZI as a sequence of a coupler, a relative phase shift, and a coupler.

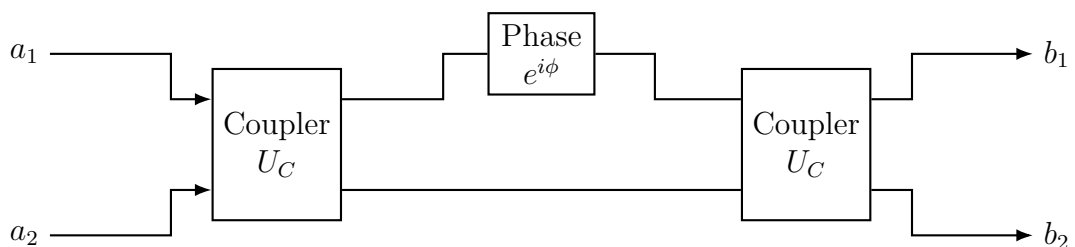


Figure 2.8: Mach-Zehnder interferometer structure for two path modes

### 2.5.2 MZI Transformation

We use the coupler matrix  $U_C(\kappa)$  and a relative phase shifter  $U_\phi$ . The overall MZI transformation is

$$U_{\text{MZI}}(\kappa, \phi) = U_C(\kappa) U_\phi U_C(\kappa), \quad U_\phi = \begin{pmatrix} 1 & 0 \\ 0 & e^{i\phi} \end{pmatrix}. \quad (2.53)$$

### 2.5.3 Ideal 50:50 Couplers

For an ideal 50 : 50 coupler,  $\kappa = \pi/4$ . In this case,

$$U_C\left(\frac{\pi}{4}\right) = \frac{1}{\sqrt{2}} \begin{pmatrix} 1 & i \\ i & 1 \end{pmatrix}. \quad (2.54)$$

Substituting this into the MZI expression gives

$$U_{\text{MZI}}\left(\frac{\pi}{4}, \phi\right) = \frac{1}{2} \begin{pmatrix} 1 - e^{i\phi} & i(1 + e^{i\phi}) \\ i(1 + e^{i\phi}) & -1 + e^{i\phi} \end{pmatrix}. \quad (2.55)$$

### 2.5.4 Bar and Cross States

We define the bar state as the condition where each input exits from the same-index output port, and we define the cross state as the condition where each input exits from the opposite output port.

For  $\phi = 0$ ,

$$U_{\text{MZI}}\left(\frac{\pi}{4}, 0\right) = \begin{pmatrix} 0 & i \\ i & 0 \end{pmatrix}, \quad (2.56)$$

which corresponds to the cross state up to a global phase.

For  $\phi = \pi$ ,

$$U_{\text{MZI}}\left(\frac{\pi}{4}, \pi\right) = \begin{pmatrix} 1 & 0 \\ 0 & -1 \end{pmatrix}, \quad (2.57)$$

which corresponds to the bar state up to a relative phase.

### 2.5.5 Switching by Phase Control

These results show that controlling the relative phase  $\phi$  enables switching between cross and bar behavior. We use this principle as the basis for an elementary  $2 \times 2$  optical switch in the following chapters.

## 2.6 Quantum Network Scalability and the Need for Switching

### 2.6.1 Quantum Network View

A quantum network connects distant quantum nodes using photonic links. In this thesis, switching is used to select and reconfigure optical paths between nodes and links.

### 2.6.2 Why Switching is Needed

As the number of nodes increases, the number of possible connections also increases. A fixed point-to-point layout does not provide flexible routing. An optical switch enables dynamic path selection, so the same hardware can support multiple connection patterns.

### 2.6.3 Elementary $2 \times 2$ Switch

We treat a  $2 \times 2$  switch as an elementary building block. A large switching network can be constructed by cascading multiple  $2 \times 2$  switches. This modular approach supports scalable architectures and allows performance to be analyzed from the behavior of the elementary unit.

# Chapter 3

## Problem Definition

### 3.1 Scope and Goal

We address the design of an integrated  $2 \times 2$  optical switch operating near 422 nm for trapped-ion quantum networking. This chapter defines the switching task, identifies dominant constraints at visible wavelengths, and sets quantitative performance targets that guide the design and simulation in the next chapter.

We use a Mach-Zehnder interferometer as the switching primitive. We define requirements at the level of a single  $2 \times 2$  element while considering that practical networks require cascading many such elements.

### 3.2 System Flow and Interface Assumptions

Our target use case is a trapped-ion quantum network where a single photon emitted by an ion is collected, delivered through free-space optics and fiber, encoded, and routed by an integrated switching fabric.

We assume the following end-to-end flow. A trapped-ion node emits a single photon near 422 nm. The photon is prepared in a polarization qubit at the node side. A polarization-to-time-bin encoder converts the polarization qubit into a time-bin qubit using bulk optics. The time-bin qubit is then routed by the integrated  $2 \times 2$  MZI switch chip and used as a building block for a scalable switching network.

### 3.3 Trapped-Ion Platform

A trapped-ion qubit is stored in an internal electronic states of a single ion confined by radio-frequency electric fields in a linear Paul trap. The qubit is initialized by

optical pumping, manipulated by resonant drives, and read out by state-dependent fluorescence.

Photons provide the interface between stationary ion qubits and flying photonic qubits. In remote entanglement protocols, photons emitted from separate ions interfere at a beam splitter and are detected to herald entanglement. This thesis focuses on the photonic routing component that sits between ion-photon interfaces and the network fabric.

### 3.4 Why 422 nm is Not the Telecom Problem

Telecom-band integrated switching benefits from low-loss fiber coupling, packaging, and standardized components. By contrast, operation near 422 nm shifts the dominant limitations.

First, scattering from sidewall roughness is stronger at shorter wavelengths and tends to dominate propagation loss. Second, fabrication tolerances tighten because small geometric deviations produce larger effective-index shifts and phase errors in units of optical wavelength. Third, visible-band coupling and packaging are less standardized, and mode sizes are smaller, which increases sensitivity to alignment and mode mismatch.

In addition, trapped-ion photons are often narrowband compared to many telecom photonic sources. Narrow linewidth increases sensitivity to phase noise and revealed imbalance in interferometric circuits. This makes phase stability and arm matching central to a switch that must preserve coherent qubit information.

### 3.5 Photonic Qubit Constraint

We require the switch to be compatible with time-bin photonic qubits. A time-bin qubit carries information in the relative amplitude and relative phase between early and late temporal modes. Therefore, a valid switching operation must route both bins consistently and preserve coherence across the time-bin separation.

This requirement turns device-level imperfections into qubit-level errors. Differential loss between arms reduces interference visibility. Uncontrolled phase drift degrades state fidelity. Polarization-dependent behavior can couple the intended qubit space to unwanted modes and reduce coherence.

## 3.6 Switching Task Definition

The device has two inputs and two outputs and operates in two states. In the bar state, each input exits from the output port with the same index. In the cross state, each input exits from the opposite output port. Switching is implemented by controlling the relative phase between the interferometer arms.

For time-bin qubits, the same routing rule must hold for the early and late bins. Any time-dependent distortion or state-dependent routing increases error rates in a cascaded switching fabric.

## 3.7 Loss Budget and Switch Chip Structure

### 3.7.1 Loss Budget at 422 nm

In a quantum network, optical loss directly reduces the success probability of distributing entanglement. Loss also compounds when multiple switching elements are cascaded. For this reason, we define a loss budget for a single  $2 \times 2$  switch element and treat it as a primary design constraint.

We express the insertion loss of one switch element as a sum of contributions

$$IL_{\text{tot}} = IL_{\text{fc}} + IL_{\text{MMI}} + IL_{\text{prop}} + IL_{\text{EO}} + IL_{\text{bend}} + IL_{\text{other}}. \quad (3.1)$$

Here, each term corresponds to a physical origin that can be independently optimized or bounded.

**Fiber-to-chip coupling loss  $IL_{\text{fc}}$ .** This term accounts for mode mismatch and alignment tolerance between the external optical fiber mode and the on-chip waveguide mode. At 422 nm, coupling is generally more sensitive because guided modes are smaller and visible-band packaging components are less standardized than telecom-band components.

**Splitter and combiner excess loss  $IL_{\text{MMI}}$ .** We implement the input splitter and output combiner using  $2 \times 2$  multimode interference components.  $IL_{\text{MMI}}$  captures excess loss in these elements beyond the ideal power division and recombination. This term includes loss from imperfect self-imaging, fabrication-induced imbalance, and scattering in the multimode region.

**Propagation loss  $IL_{\text{prop}}$ .** Propagation loss accumulates along the total optical path length through the interferometer arms and interconnect waveguides. At visible wave-

lengths, scattering from sidewall roughness can dominate this contribution. Because propagation loss scales with length, it directly couples to footprint and routing choices.

**Electro-optic phase shifter loss  $IL_{\text{EO}}$ .** The electro-optic phase shifter introduces loss through electrode-related absorption, additional scattering from altered waveguide geometry, and any overlap between the optical mode and lossy regions near the electrodes. Although lithium niobate provides efficient phase tuning via the Pockels effect, electrode design and placement must be chosen to minimize optical attenuation.

**Bend loss  $IL_{\text{bend}}$ .** Bend loss occurs when waveguides curve and the optical mode radiates or couples to higher-order or radiation modes. At shorter wavelengths, tighter bends may be feasible in footprint but can still introduce non-negligible excess loss if the bend radius approaches the confinement limit.

**Other losses  $IL_{\text{other}}$ .** This term collects smaller contributions that are not easily isolated at the block level. Examples include transitions between straight and bend sections, junction losses at component interfaces, and polarization-dependent loss that manifests as apparent attenuation in the measured port power.

**Target loss range.** We set a design target of

$$IL_{\text{tot}} \leq 3 \text{ dB} \quad (3.2)$$

as an ideal goal for a single switch element. We also define an acceptable range up to

$$IL_{\text{tot}} \leq 5 \text{ dB}, \quad (3.3)$$

which provides a realistic tolerance while still enabling cascaded operation in moderate-depth switching networks.

### 3.7.2 MZI Switch Chip Structure

We implement the  $2 \times 2$  switch using a Mach-Zehnder interferometer integrated on lithium niobate. The device is composed of the following building blocks.

**Input and output couplers.** Light enters and exits the chip through fiber-to-chip interfaces. These couplers define the external insertion loss baseline and strongly affect packaging tolerance at 422 nm. In the loss budget, their contribution is captured by  $IL_{\text{fc}}$ .

**$2 \times 2$  MMI splitter and combiner.** We use a  $2 \times 2$  MMI at the input to split optical power into two arms and a second  $2 \times 2$  MMI at the output to recombine the arms. Ideally, these MMIs provide balanced mixing to enable high-contrast interference at the output ports. Deviations from ideal mixing increase crosstalk and reduce extinction ratio, while excess loss contributes to  $IL_{\text{MMI}}$ .

**Electro-optic phase shifter.** We place an electro-optic phase shifter on one interferometer arm to control the relative phase between the arms. This control enables switching between bar and cross states. The phase shifter also introduces an incremental loss contribution  $IL_{\text{EO}}$ , which must be minimized through electrode geometry and placement.

**Two LN waveguide arms with an imbalance-free design intent.** The interferometer consists of two lithium-niobate waveguide arms that are designed to be equal in optical path length. This symmetry makes the output depend primarily on a controllable phase difference rather than on fixed geometric mismatch. In our  $2 \times 2$  switching MZI, we intentionally avoid a delay-line imbalance, since time-bin separation is created in the polarization-to-time-bin converter instead of inside the switch.

The switching operation is determined by the relative phase between the two arms. We introduce this phase difference using an electro-optic phase shifter while keeping the remaining arm geometry as symmetric as possible. Any residual imbalance in path length or loss reduces interference visibility and degrades the extinction ratio, effectively increasing crosstalk in the bar and cross states.

#### Summary of structure.

I/O coupler →  $2 \times 2$  MMI splitter → two LN arms with EO phase control →  
 $2 \times 2$  MMI combiner → I/O coupler

This block-level description provides a direct mapping between physical components and the loss budget in Eq. (3.1).

## 3.8 Material Platform and Justification: Lithium Niobate

We choose lithium niobate as the platform because it provides strong electro-optic phase control and supports interferometric circuits with electrical tuning. Electro-optic tuning is attractive for switching because it can provide fast response and avoids slow thermal time constants.

At 422 nm, the same platform introduces additional constraints. Fabrication quality and sidewall roughness directly set the propagation loss. Polarization behavior must be controlled because birefringence variations translate into phase errors. Coupling and packaging must handle smaller mode sizes and visible-band components.

Table 3.1 summarizes a comparison of material platforms.

	$\text{SiO}_2$	Si	$\text{LiNbO}_3$
Classification	Dielectric insulator	Semiconductor	Strong dielectric
Refractive index	1.45	3.5	2.2
Mechanism	Thermo-optic	Thermo-optic	Pockels electro-optic
What is controlled	Temperature controls phase	Temperature controls phase	Voltage controls phase
Waveguide propagation loss	Below 0.05 dB cm <sup>-1</sup>	About 1.5 dB cm <sup>-1</sup>	About 0.1 to 0.2 dB cm <sup>-1</sup>
Fiber coupling loss	Below 1 dB	About 2 to 5 dB	About 1 to 5 dB
Switching speed	kHz to MHz	kHz using heaters	GHz
Device examples	Passive interferometers	Integrated photonic circuits	Electro-optic modulators and switches

Table 3.1: Comparison of integrated photonics material platforms

## 3.9 Problem Statement

We define the problem addressed in this thesis as follows.

- We design an integrated  $2 \times 2$  MZI optical switch operating near 422 nm.
- We require bar and cross states controlled by a tunable relative phase.
- We require compatibility with time-bin photonic qubits, preserving coherence and relative phase through the switching operation.

- We evaluate feasibility under lithium niobate constraints at visible wavelengths.
- We quantify performance using insertion loss ( $IL$ ), extinction ratio ( $ER$ ), and crosstalk ( $XT$ )

# Chapter 4

## Method and Design

### 4.1 Ansys Simulation Workflow

In this chapter, we model a lithium-niobate Mach-Zehnder interferometer switch operating near 422 nm using Ansys Lumerical. We aim to evaluate device-level performance metrics including the Pockels electro-optic effect. To do so, we use a multi-stage workflow that connects optical mode solving, electrostatic field solving, and circuit-level propagation.

#### 4.1.1 Overview of the Flow

We adopt the following solver sequence:

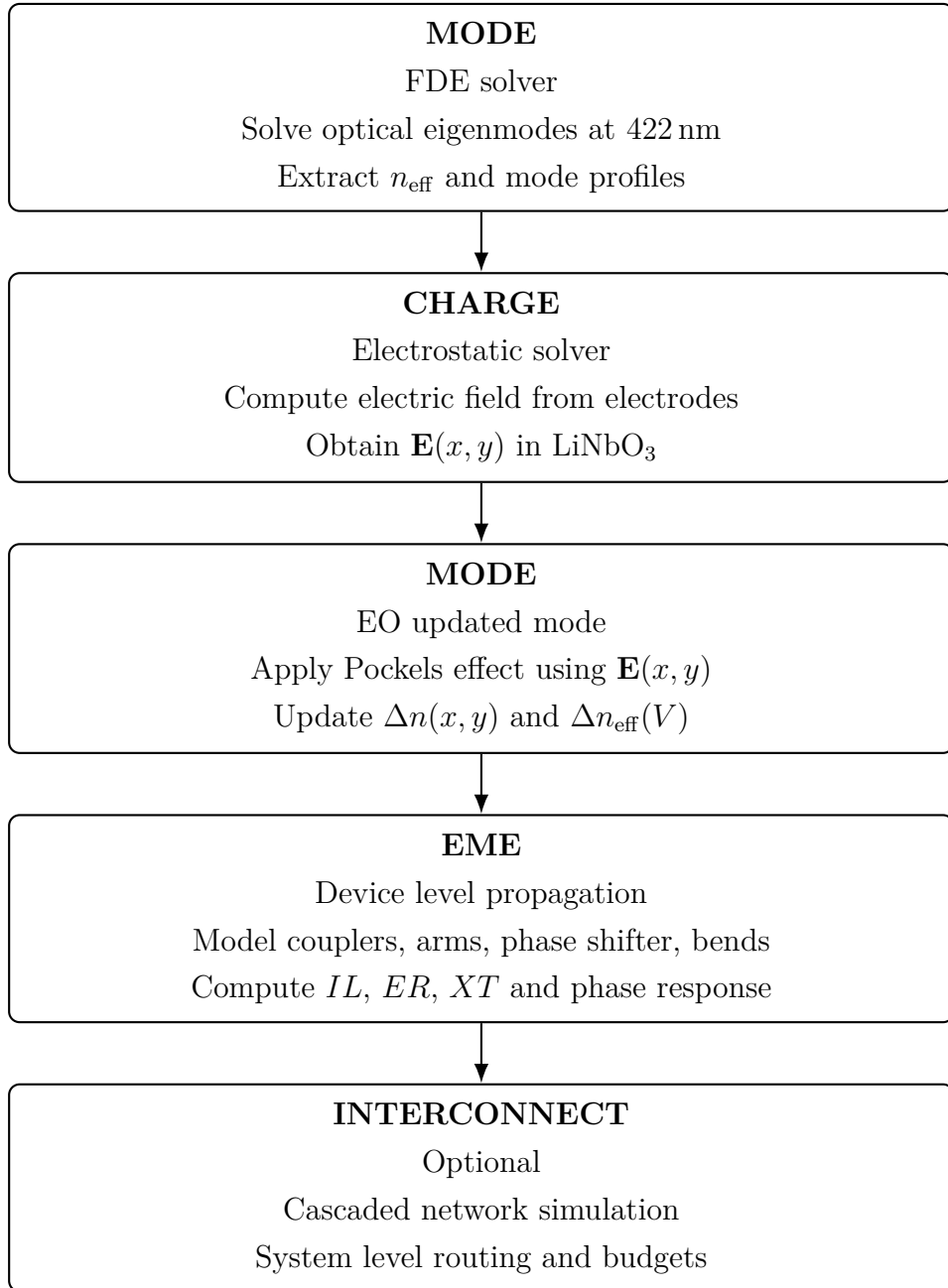


Table 4.1: Overview flow of simulation

Each solver plays a distinct role. MODE is used to obtain optical modes and effective indices at 422 nm. CHARGE computes the static electric-field distribution created by electrodes. The EO update step in MODE converts the electric field into a refractive-index perturbation through the Pockels effect, enabling the extraction of voltage-dependent phase shift. EME then propagates fields through the full MZI geometry and yields port-to-port transmission, from which we compute insertion loss, extinction ratio, and crosstalk. INTERCONNECT is optionally used for cascading many  $2 \times 2$  elements and estimating system-level scaling.

### 4.1.2 Common Geometry and Parameter Definition

Before running the solvers, we fix a consistent set of geometrical and physical parameters that are shared across MODE, CHARGE, and EME. Key parameters include the target wavelength, the lithium-niobate crystal cut and axis convention, and the polarization basis used in the switch. We also define the waveguide cross-section and cladding configuration, electrode dimensions and spacing, and the MZI layout parameters such as arm lengths, bend radii, and the splitter/combiner geometry. This shared parameterization enables consistent sweeps.

### 4.1.3 MODE FDE Step 1: Optical Modes and Baseline Loss

MODE with the finite-difference eigenmode solver provides the optical mode solutions for the waveguide cross-sections at 422 nm. We use this step to obtain the baseline effective index and propagation loss of straight waveguides, bends, and the EO phase-shifter cross-section.

**Step 1: Build cross-sections.** We construct the cross-sections required for the circuit. This includes a straight LN waveguide cross-section and a phase-shifter cross-section that includes the buffer layer and electrodes. We ensure the material dispersion model is consistent at 422 nm.

**Step 2: Solve for guided modes.** We solve for the fundamental guided mode and record its effective index  $n_{\text{eff}}$ , mode field profile, and any computed propagation loss. We also check that the mode polarization is consistent with the intended device operation.

**Step 3: Export data for later stages.** We save the mode profiles and indices to be used as port modes in EME. This ensures that EME power normalization and overlap calculations remain consistent.

### 4.1.4 CHARGE: Electrostatic Field of the EO Phase Shifter

CHARGE computes the electrostatic potential and electric-field distribution produced by the electrode geometry. This field distribution is required to model the Pockels effect in lithium niobate.

**Step 1: Build the electrostatic model.** We build a 2D cross-sectional or 3D electrode model of the phase-shifter region. A cross-sectional electrostatic model is

sufficient when the electrode structure is invariant along the propagation direction. We use a 3D model only if fringing fields and longitudinal variations are essential.

**Step 2: Assign materials and boundary conditions.** We assign appropriate permittivities to dielectric regions and define the electrodes as conductors. We set one electrode to the drive voltage  $V$  and the other to ground.

**Step 3: Solve and export electric fields.** We solve for the electrostatic potential and export the electric field components  $E_x$ ,  $E_y$ , and  $E_z$  in the lithium-niobate region. We verify the coordinate convention so that field directions are correctly interpreted in the EO tensor mapping.

#### 4.1.5 MODE FDE Step 2: Pockels Effect and $V_\pi L$ Extraction

We include the Pockels effect by converting the CHARGE-computed electric field into a refractive-index perturbation. This enables us to extract a voltage-dependent effective index and phase shift.

**Step 1: Define crystal axes and EO tensor.** Lithium niobate is anisotropic, and the EO response depends on the crystal orientation. We define the LN axis convention and apply the appropriate EO tensor coefficients.

**Step 2: Map electrostatic fields onto the optical mesh.** We import the CHARGE field distribution and map it onto the MODE cross-section. We verify that the spatial alignment between CHARGE and MODE is correct.

**Step 3: Compute  $\Delta n_{\text{eff}}(V)$  and phase shift.** For each applied voltage  $V$ , MODE yields an updated effective index. We compute the voltage-dependent phase shift over a phase-shifter length  $L$  as

$$\phi(V) = \frac{2\pi}{\lambda} \Delta n_{\text{eff}}(V) L. \quad (4.1)$$

The half-wave voltage-length product is extracted by solving

$$\phi(V_\pi) = \pi, \quad V_\pi L = \frac{\pi\lambda}{2\pi \Delta n_{\text{eff}}(V)/V}. \quad (4.2)$$

We also quantify any additional optical loss induced by electrode proximity, since it directly contributes to the switch loss budget.

### 4.1.6 EME: Full MZI Propagation and Switching Metrics

EME propagates optical fields through the full device structure and provides the port-to-port transmission of the  $2 \times 2$  switch. We construct the MZI from its physical blocks, including the  $2 \times 2$  splitter, two arms, EO phase-shifter section, and the  $2 \times 2$  combiner.

**Step 1: Define ports and input modes.** We set the input and output ports and specify the port modes using the MODE results. This ensures that the transmitted powers correspond to coupling into the correct guided modes.

**Step 2: Assemble the circuit geometry.** We implement the splitter and combiner using the chosen coupling element. We then include two waveguide arms, where one arm contains the EO phase shifter that introduces a controllable phase  $\phi(V)$ .

**Step 3: Sweep the control voltage and compute transmission.** We sweep the drive voltage  $V$ , which maps to a phase shift  $\phi(V)$ . For each voltage point, EME returns the complex transmission from each input to each output. From these, we compute insertion loss, extinction ratio, and crosstalk.

#### Insertion Loss

For a selected switching state, insertion loss is computed from the transmitted power to the intended output:

$$IL = -10 \log_{10} \left( \frac{P_{\text{out,desired}}}{P_{\text{in}}} \right). \quad (4.3)$$

#### Extinction Ratio and Crosstalk

Extinction ratio compares the desired output power to the undesired output power:

$$ER = 10 \log_{10} \left( \frac{P_{\text{out,desired}}}{P_{\text{out,undesired}}} \right). \quad (4.4)$$

Crosstalk quantifies leakage to the unintended port:

$$XT = 10 \log_{10} \left( \frac{P_{\text{out,undesired}}}{P_{\text{in}}} \right). \quad (4.5)$$

#### Phase Stability and Imbalance Sensitivity

We evaluate sensitivity to imbalance by introducing controlled perturbations to the two arms, including path-length mismatch and loss mismatch. We then quantify the

resulting degradation in extinction ratio and switching contrast as a function of these perturbations.

#### 4.1.7 INTERCONNECT Optional: Cascaded Switching Networks

For system-level scaling studies, we optionally use INTERCONNECT. We create compact block models of the  $2 \times 2$  switch using the EME-derived scattering parameters and voltage-phase relationships. This allows rapid simulation of cascaded networks and loss compounding across many switching stages. We use this step only when analyzing scalability beyond a single device.

#### 4.1.8 Summary of Extracted Quantities

The workflow yields the following key outputs:

- Baseline waveguide and component losses at 422 nm from MODE and EME
- EO phase response  $\Delta n_{\text{eff}}(V)$ ,  $\phi(V)$ , and  $V_{\pi}L$  from CHARGE and MODE
- Switch-level performance metrics  $IL$ ,  $ER$ , and  $XT$  from EME
- Sensitivity to imbalance and drift via parameter sweeps
- Optional cascaded-network behavior using INTERCONNECT

# Chapter 5

## Evaluation

### 5.1 MODE

This section evaluates the guided optical modes of the LNOI ridge waveguide cross-section using the eigenmode solver (FDE) in Ansys Lumerical MODE at  $\lambda = 422$  nm. The objective is to (i) confirm the existence of a physically guided fundamental mode ( $\text{TE}_0$ ), (ii) extract modal parameters ( $n_{\text{eff}}$ , loss,  $A_{\text{eff}}$ , polarization fraction), and (iii) establish the baseline optical mode required for subsequent electro-optic (EO) efficiency evaluation.

#### 5.1.1 Material Declaration

Lithium niobate (LN or  $\text{LiNbO}_3$ ) is a uniaxial birefringent crystal. In the optical model, LN is represented as an anisotropic dielectric with diagonal permittivity tensor. The ordinary and extraordinary refractive indices at the operating wavelength are denoted as  $n_o(\lambda)$  and  $n_e(\lambda)$ , respectively.

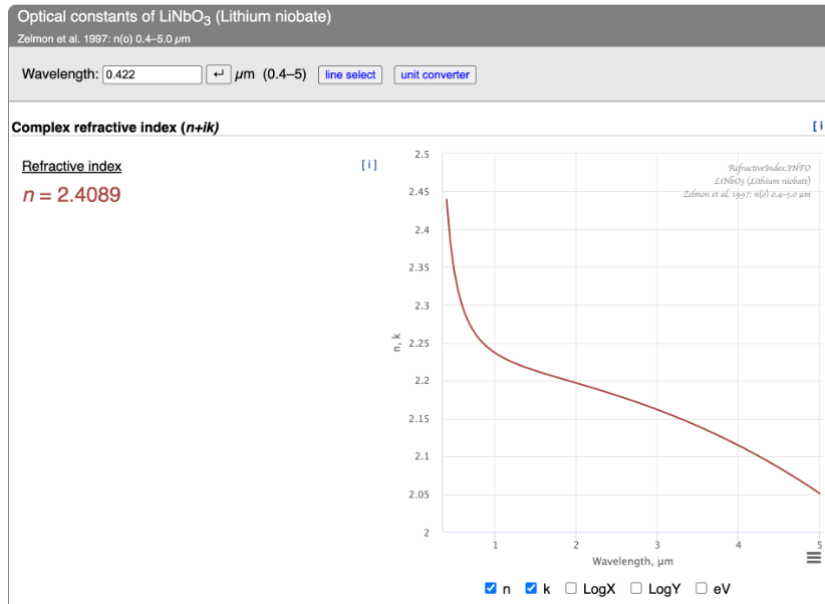


Figure 5.1: Reference dispersion of LiNbO<sub>3</sub> ordinary refractive index  $n_o(\lambda)$ . At  $\lambda = 0.422 \mu\text{m}$ ,  $n_o = 2.4089$ .

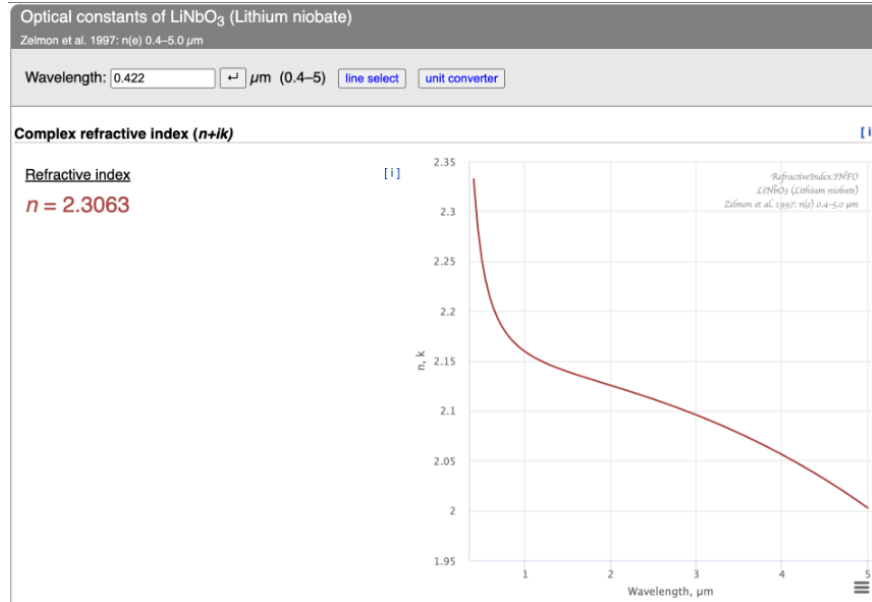


Figure 5.2: Reference dispersion of LiNbO<sub>3</sub> extraordinary refractive index  $n_e(\lambda)$ . At  $\lambda = 0.422 \mu\text{m}$ ,  $n_e = 2.3063$ .

### 5.1.2 Sellmeier Equation

The Sellmeier equation is an empirical dispersion model that expresses the wavelength-dependent refractive index  $n(\lambda)$  as a rational function of  $\lambda$ . In the 3-term Sellmeier

form used here,

$$n^2(\lambda) = A_0 + \sum_{i=1}^3 \frac{B_i \lambda^2}{\lambda^2 - C_i}, \quad (5.1)$$

where  $A_0$ ,  $B_i$ , and  $C_i$  are fitting coefficients. We apply Eq. (5.1) separately to the ordinary and extraordinary indices. The ordinary ( $n_o$ ) and extraordinary ( $n_e$ ) indices are written as:

$$n_o^2(\lambda) = 1 + \frac{2.6734 \lambda^2}{\lambda^2 - 0.01764} + \frac{1.2290 \lambda^2}{\lambda^2 - 0.05914} + \frac{12.614 \lambda^2}{\lambda^2 - 474.6}, \quad (5.2)$$

$$n_e^2(\lambda) = 1 + \frac{2.9804 \lambda^2}{\lambda^2 - 0.02047} + \frac{0.5981 \lambda^2}{\lambda^2 - 0.0666} + \frac{8.9543 \lambda^2}{\lambda^2 - 416.08}. \quad (5.3)$$

### 5.1.3 Material Declaration in FDE

To incorporate LiNbO<sub>3</sub> birefringence in the eigenmode (FDE) simulations, we declared a custom material “LiNbO<sub>3</sub>\_xcut\_20C” with diagonal anisotropy and assigned Sellmeier coefficients from Eq. (5.2) and Eq. (5.3) to each principal axis:

$$n_{xx}(\lambda) = n_{yy}(\lambda) = n_o(\lambda), \quad n_{zz}(\lambda) = n_e(\lambda). \quad (5.4)$$

Figure 5.3 shows the coefficient table used in the material editor. The  $xx$  and  $yy$  columns share identical coefficients (ordinary index), while the  $zz$  column uses the extraordinary-index coefficients.

Material Properties - LiNbO <sub>3</sub> _xcut_20C			
	xx	yy	zz
A0	1	1	1
B1	2.6734	2.6734	2.9804
C1 (microns <sup>2</sup> )	0.01764	0.01764	0.02047
B2	1.229	1.229	0.5981
C2 (microns <sup>2</sup> )	0.05914	0.05914	0.0666
B3	12.614	12.614	8.9543
C3 (microns <sup>2</sup> )	474.6	474.6	416.08

Figure 5.3: Custom material declaration in Lumerical for LiNbO<sub>3</sub>\_xcut\_20C using a diagonal anisotropic Sellmeier model. Coefficients for  $xx$  and  $yy$  correspond to  $n_o(\lambda)$ , and those for  $zz$  correspond to  $n_e(\lambda)$ .

### 5.1.4 Verification Using Material Explorer

After declaring the material, we verified that the material explorer reproduces the intended refractive index values around the target wavelength. Figures 5.4 and 5.5 show the real part of the refractive index plotted versus wavelength for the  $xx/yy$  (ordinary) and  $zz$  (extraordinary) components, respectively. At  $\lambda \approx 0.422 \mu\text{m}$ , the extracted values match the reference indices (i.e.,  $n_o \simeq 2.4089$  and  $n_e \simeq 2.3063$ ), confirming that the Sellmeier coefficients were correctly implemented.

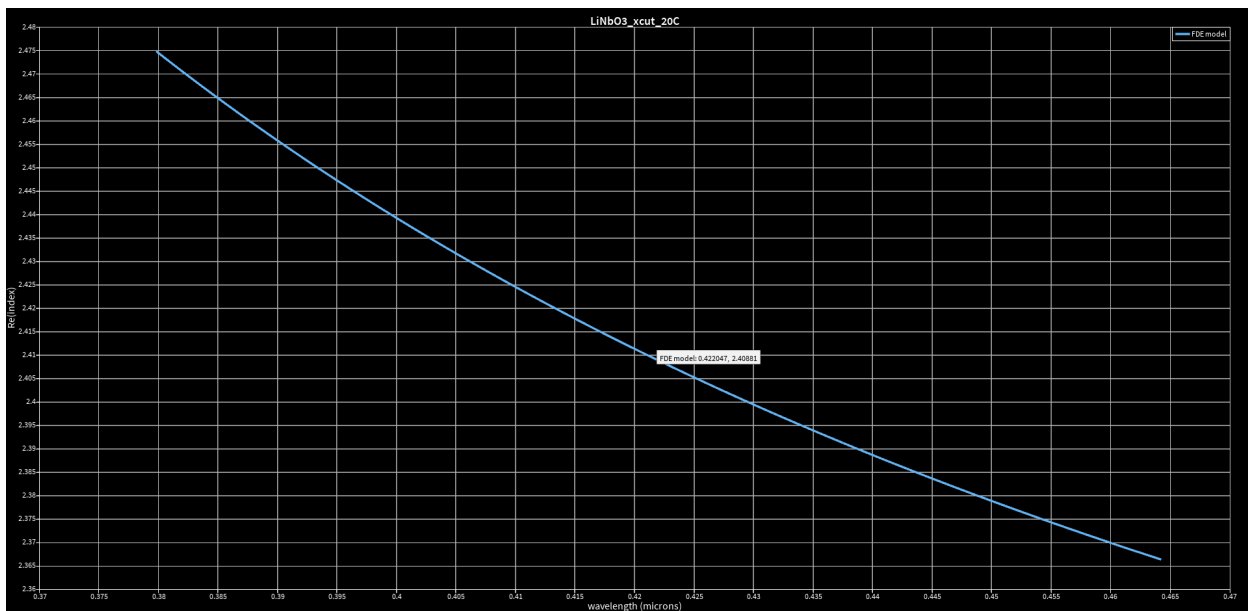


Figure 5.4: Material explorer check for the declared LiNbO<sub>3</sub>\_xcut\_20C material: ordinary-index component ( $xx/yy$ ). The value at  $\lambda \approx 0.422 \mu\text{m}$  matches  $n_o \simeq 2.4089$ .

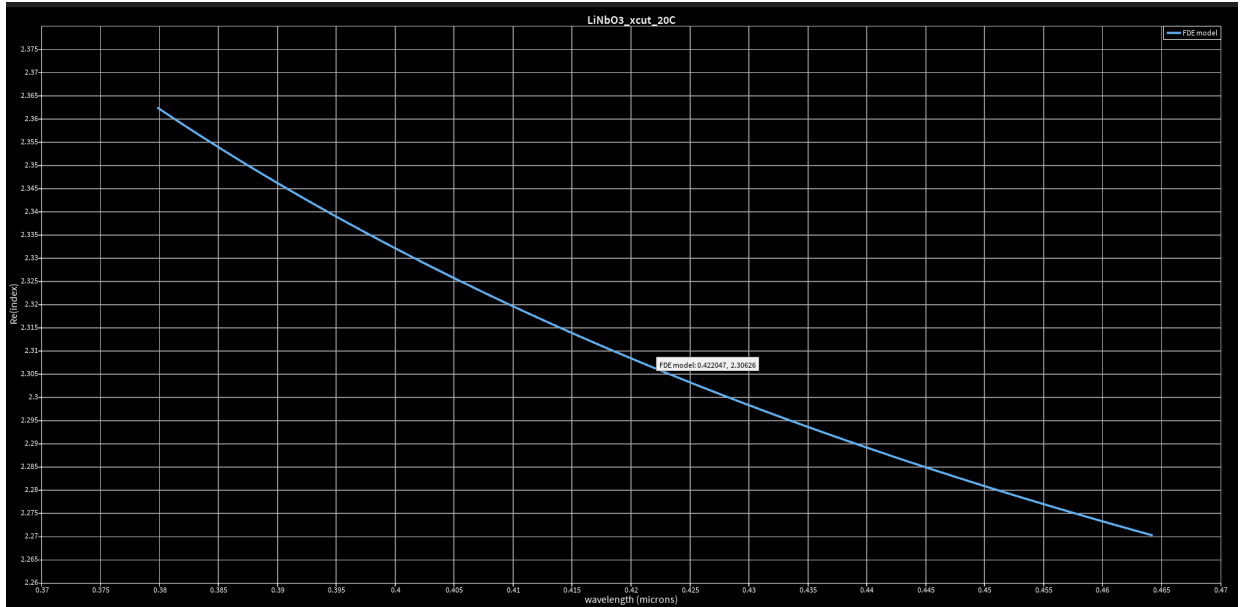


Figure 5.5: Material explorer check for the declared  $\text{LiNbO}_3\text{-}x\text{cut}\text{-}20\text{C}$  material: extraordinary-index component ( $zz$ ). The value at  $\lambda \approx 0.422 \mu\text{m}$  matches  $n_e \simeq 2.3063$ .

### 5.1.5 Waveguide Cross-section Geometry in MODE

The eigenmodes of the LNOI ridge waveguide were computed using Ansys Lumecrical MODE (FDE solver). The propagation direction is set to the  $z$ -axis, and the waveguide cross-section is defined in the  $x-y$  plane. Figure 5.6 shows the object tree and the 2D/3D views of the modeled cross-section. The geometry consists of three rectangular primitives: (i) a buried oxide (BOX) layer, (ii) an  $\text{LiNbO}_3$  slab layer, and (iii) an etched ridge region on top of the slab.

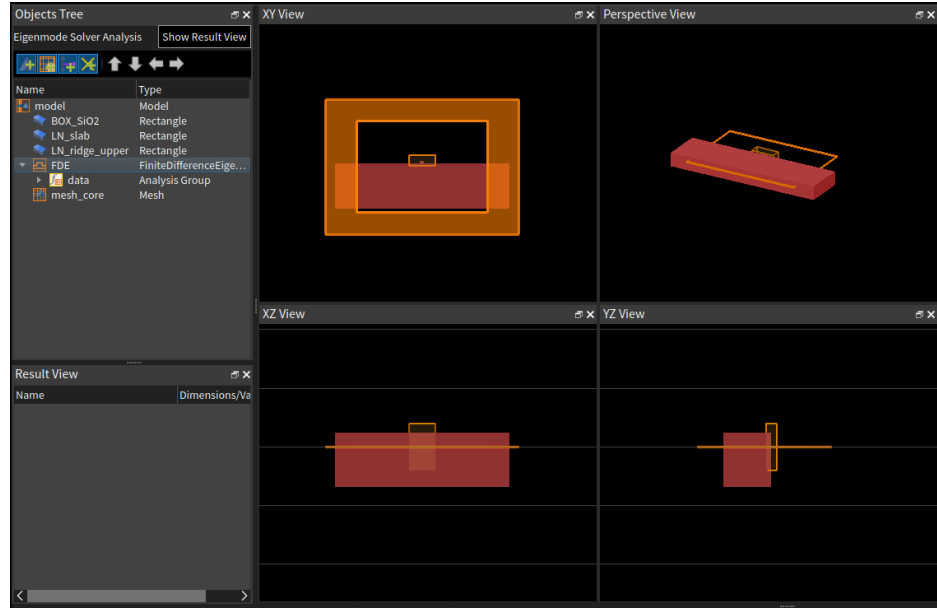


Figure 5.6: Geometry objects and material assignments in MODE.

### 5.1.6 Objects and Assigned Materials

Table 5.1 summarizes the geometric objects used in the MODE model, together with their material assignments. The LiNbO<sub>3</sub> regions (slab and ridge) use the custom anisotropic Sellmeier material (LiNbO<sub>3</sub>\_xcut\_20C) introduced in Fig. 5.3, while the BOX region uses SiO<sub>2</sub>.

Table 5.1: Geometry objects and material assignments in MODE

Object name	Type	Material	Role
BOX_SiO2	Rectangle	SiO <sub>2</sub>	Buried oxide (lower cladding)
LN_slab	Rectangle	LiNbO <sub>3</sub> _xcut_20C	LiNbO <sub>3</sub> thin film (slab)
LN_ridge_upper	Rectangle	LiNbO <sub>3</sub> _xcut_20C	Ridge (etched defining core)

### 5.1.7 Geometrical Parameters

Each rectangle is specified by its span in  $(x_{\min}, x_{\max}, y_{\min}, y_{\max})$  in the  $x-y$  plane. In the present work, these parameters were chosen such that (1) the computational window encloses the full optical field with sufficient margin and (2) the ridge and slab alignment reproduces the intended LNOI ridge waveguide cross-section. For clarity, we report the

geometry using the following parameterization (all coordinates are given in  $\mu\text{m}$ ):

$$\text{BOX\_SiO}_2: \quad x \in [-4, 4], \quad y \in [-2, 0], \quad (5.5)$$

$$\text{LN\_slab:} \quad x \in [-4, 4], \quad y \in [0, 0.06], \quad (5.6)$$

$$\text{LN\_ridge\_upper:} \quad x \in [-0.1, 0.1], \quad y \in [0.06, 0.18]. \quad (5.7)$$

As a result, final sweep of the geometry can be defined as

$$w = x_{\max}^{\text{ridge}} - x_{\min}^{\text{ridge}} = 0.1 - (-0.1) = 0.2 \mu\text{m}, \quad (5.8)$$

$$h = y_{\max}^{\text{ridge}} - y_{\min}^{\text{ridge}} = 0.18 - 0.06 = 0.12 \mu\text{m}. \quad (5.9)$$

For reference, the slab thickness is  $t_{\text{slab}} = 0.06 \mu\text{m}$  and the total LN thickness is  $t_{\text{LN,tot}} = 0.18 \mu\text{m}$ .

### 5.1.8 FDE Eigenmode Calculation Settings and its Result

The guided modes were computed using the finite-difference eigenmode (FDE) solver at the design wavelength  $\lambda = 0.422 \mu\text{m}$ . The solver was configured to search for guided solutions near a user-specified effective index, and multiple trial modes were computed to identify the fundamental TE-like mode ( $\text{TE}_0$ ). Figure 5.7 summarizes the key solver settings and the resulting modal field visualization.

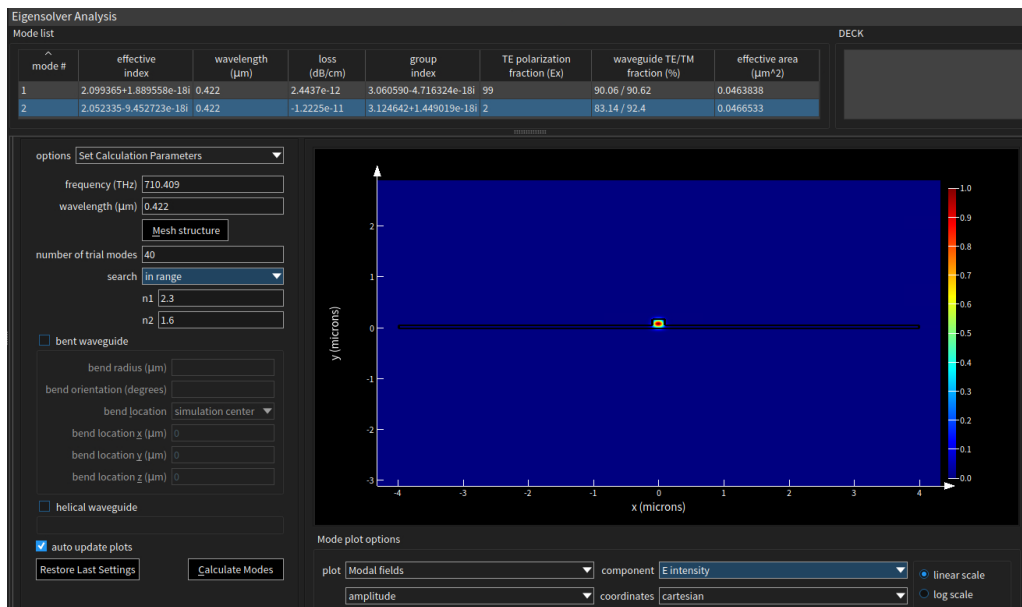


Figure 5.7: MODE calculation settings and field plot at  $\lambda = 0.422 \mu\text{m}$ . The displayed plot shows the electric-field intensity ( $|E|^2$ ) distribution in the  $x$ - $y$  cross-section.

The principal parameters used for the eigenmode calculation are:

- Wavelength:  $\lambda = 0.422 \mu\text{m}$ .
- Number of trial modes: 40.
- Mode search method: `in range` with  $n_{\text{eff}} \in [n_2, n_1] = [1.6, 2.3]$ .
- Field visualization: `Modal fields`, component `E intensity` ( $|E|^2$ ).

The `in range` setting does not modify the waveguide/material properties; it constrains the eigensolver to search for solutions whose effective index falls within the specified interval. The range [1.6, 2.3] was selected to bracket the expected  $n_{\text{eff}}$  of guided modes, typically  $n_{\text{clad}} < n_{\text{eff}} < n_{\text{core}}$ .

Among the computed solutions, the fundamental TE-like mode ( $\text{TE}_0$ ) corresponds to mode #1 in Fig. 5.7, as indicated by a high TE polarization fraction (Ex) of 99%. The key numerical outputs for  $\text{TE}_0$  at  $\lambda = 0.422 \mu\text{m}$  are:

$$n_{\text{eff}} \approx 2.099365 - 1.8896 \times 10^{-18}i, \quad (5.10)$$

$$\text{loss} \approx 2.4437 \times 10^{-12} \text{ dB/cm}, \quad (5.11)$$

$$A_{\text{eff}} \approx 4.63838 \times 10^{-2} \mu\text{m}^2. \quad (5.12)$$

The imaginary parts and the reported loss values on the order of  $10^{-11}$  dB/cm are numerically negligible for the present dielectric eigenmode computation.

## 5.2 CHARGE

### 5.2.1 Geometry construction in CHARGE

This subsection details how the CHARGE electrostatic cross-section is constructed, how materials are assigned to each region, and which simulation objects (simulation region, monitor, and mesh constraints) are required before running the solver. Figure 5.8 shows the full object tree and the assembled cross-sectional model used in this work.

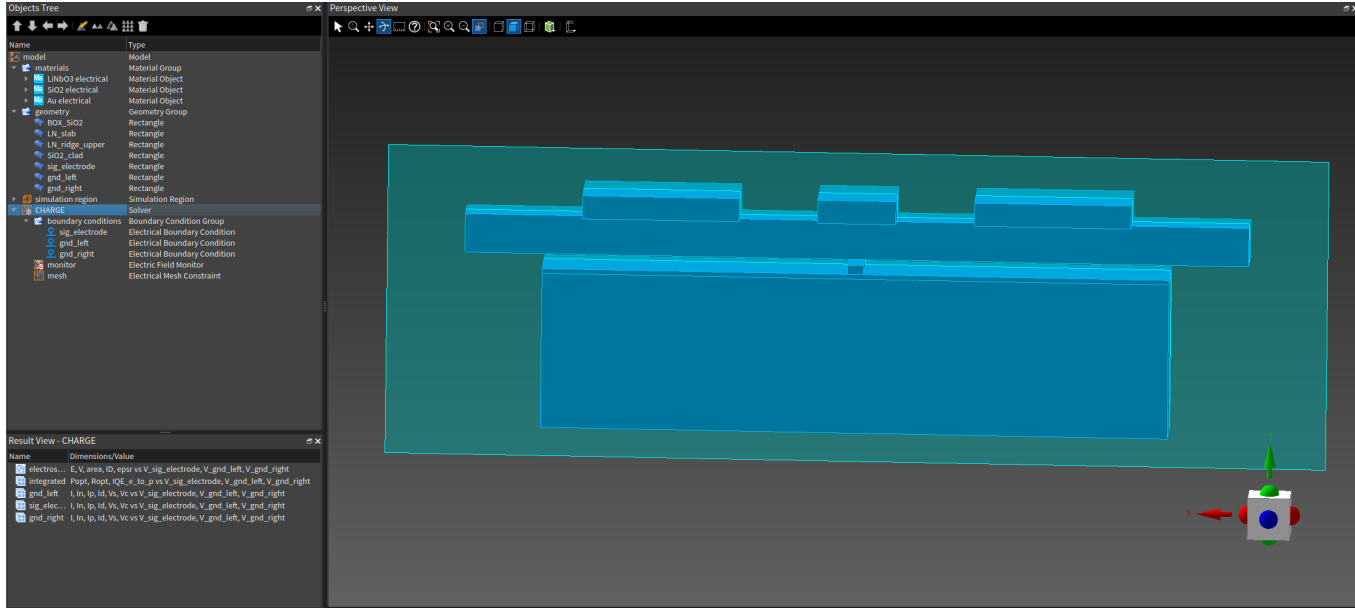


Figure 5.8: CHARGE geometry construction and object trees used for the electrostatic simulation.

**(1) Material definitions** Three electrical materials are defined in the `materials` group:

- `LiNbO3_electrical`: LiNbO<sub>3</sub> semiconductor at X/Y cut with a specified DC permittivity.
- `SiO2_electrical`: silica (SiO<sub>2</sub>) used for the BOX and the upper cladding.
- `Au_electrical`: gold (Au) used for the signal and ground electrodes.

**(2) Geometry objects and material assignment** The cross-section is created under the `geometry` group using rectangular regions. The following objects are included (Fig. 5.8):

- `BOX_SiO2` (Rectangle): buried oxide region, assigned `SiO2_electrical`.
- `LN_slab` (Rectangle): LN thin-film slab, assigned `LiNbO3_electrical`.
- `LN_ridge_upper` (Rectangle): etched ridge region on LN, assigned `LiNbO3_electrical`.
- `SiO2_clad` (Rectangle): upper SiO<sub>2</sub> cladding added for the electrical model, assigned `SiO2_electrical`.
- `sig_electrode` (Rectangle): signal electrode metal, assigned `Au_electrical`.
- `gnd_left` (Rectangle): left ground electrode metal, assigned `Au_electrical`.

- `gnd_right` (Rectangle): right ground electrode metal, assigned `Au_electrical`.

**(3) Coordinate specification** Each rectangular object is specified in the  $(x, y)$  cross-section. The bounds are recorded using minimum and maximum coordinates, where the bounds of the objects used in MODE remain equivalent (all coordinates are given in  $\mu\text{m}$ ):

$$\text{BOX\_SiO2: } x \in [-4, 4], \quad y \in [-2, 0], \quad (5.13)$$

$$\text{LN\_slab: } x \in [-4, 4], \quad y \in [0, 0.06], \quad (5.14)$$

$$\text{LN\_ridge\_upper: } x \in [-0.1, 0.1], \quad y \in [0.06, 0.18], \quad (5.15)$$

$$\text{SiO2\_clad: } x \in [-5, 5], \quad y \in [0.18, 0.68], \quad (5.16)$$

$$\text{sig\_electrode: } x \in [-0.5, 0.5], \quad y \in [0.68, 0.98], \quad (5.17)$$

$$\text{gnd\_left: } x \in [-3.5, -1.5], \quad y \in [0.68, 0.98], \quad (5.18)$$

$$\text{gnd\_right: } x \in [1.5, 3.5], \quad y \in [0.68, 0.98]. \quad (5.19)$$

**(4) Simulation region coverage** A `simulation_region` object defines the computational domain for the electrostatic solve. The region is chosen to fully enclose the BOX, LN waveguide, upper cladding, and all electrodes, with additional margins in both  $x$  and  $y$  to reduce boundary-induced distortion of the field in the waveguide region. The simulation region extent is recorded as

$$x \in [-6, 6], \quad y \in [-2.5, 1.5], \quad (5.20)$$

where the bounds are set such that the outer boundaries are sufficiently far from the electrode gap and the LN ridge.

**(5) Boundary conditions** Within the CHARGE solver object, a `boundary_conditions` group assigns electrical boundary conditions to the metal regions:

- `sig_electrode`: electrical boundary condition with prescribed potential  $V_{\text{sig}} = 1 \text{ V}$ .
- `gnd_left`: electrical boundary condition with  $V_{\text{gnd},\text{left}} = 0 \text{ V}$ .
- `gnd_right`: electrical boundary condition with  $V_{\text{gnd},\text{right}} = 0 \text{ V}$ .

This implements a single-ended drive with a signal electrode referenced to two grounded electrodes.

**(6) Monitor definition** An **E**lectric **F**ield **M**onitor (**monitor**) is added to record  $V(x, y)$  and  $\mathbf{E}(x, y)$  after the solve. The monitor is set as a 2D cross-sectional monitor spanning the region of interest (typically covering at least the full waveguide and electrode gap, and preferably most of the simulation region), with bounds

$$x \in [-2, 2], \quad y \in [-2.5, 1.2]. \quad (5.21)$$

**(7) Mesh constraint** An **E**lectrical **M**esh **C**onstraint object (**mesh**) is included to refine the discretizations near critical features such as electrode edges, electrode gap, and LN ridge. The mesh constraint region is defined to enclose the waveguide and electrode vicinity, with a finer target mesh size than the background mesh. Its extent is recorded as

$$x \in [-1, 1], \quad y \in [-0.5, 1.2]. \quad (5.22)$$

**(8) Checklists before Run** Before running CHARGE, the following items are verified:

1. All geometry objects exist and are assigned the intended electrical materials (LN/SiO<sub>2</sub>/Au).
2. The simulation region fully encloses the structure with adequate padding.
3. Electrode boundary conditions are correctly applied:  $V_{\text{sig}} = 1$  V and  $V_{\text{gnd}} = 0$  V.
4. The monitor spans the waveguide/electrode region and records  $V$ ,  $E_x$ , and  $E_y$ .
5. Mesh constraints refine the electrode-gap and LN waveguide region to avoid under-resolving the peak fields.

Once these checks pass, the electrostatic solver is executed to produce the field distributions used in the subsequent  $V_\pi L$  computation.

### 5.2.2 CHARGE results at 1 V

After the CHARGE geometry is assembled and the electrode boundary conditions are applied ( $V_{\text{sig}} = 1$  V,  $V_{\text{gnd},\text{left}} = V_{\text{gnd},\text{right}} = 0$  V), the electrostatic problem is solved to obtain the potential and electric-field distributions in the cross-section. The electric field is computed from the potential as

$$\mathbf{E}(x, y) = -\nabla V(x, y), \quad (5.23)$$

and the in-plane components  $E_x(x, y)$  and  $E_y(x, y)$  are extracted on the monitor plane for subsequent EO-overlap calculations.

**Electric-field components** Figures 5.9 and 5.10 show the corresponding field components  $E_x$  and  $E_y$  at 1 V. As expected, the strongest fields appear near electrode edges and in the electrode gap, where field crowding is most pronounced. Importantly, the field penetrates into the LN guiding region around the ridge, indicating a non-zero overlap with the optical mode. The sign of each component follows the coordinate convention of the simulation.

**Potential distribution** Figure 5.11 shows the electrostatic potential under the 1 V bias. The potential drop occurs primarily across the electrode gap region, confirming that the intended driving voltage is applied and that the simulation region captures the relevant field lines in the vicinity of the waveguide.

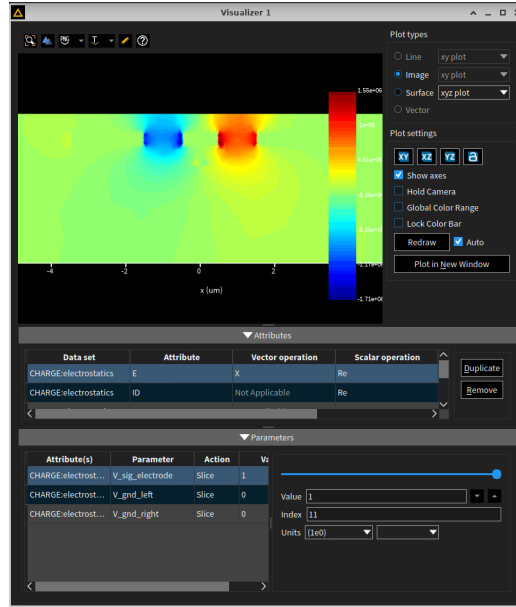


Figure 5.9: CHARGE result:  $E_x(x, y)$  distribution under a single-ended 1 V drive ( $V_{\text{sig}} = 1 \text{ V}$ ,  $V_{\text{gnd}} = 0 \text{ V}$ ). The field is concentrated near electrode edges and across the electrode gap, with a finite penetration into the LN waveguide region.

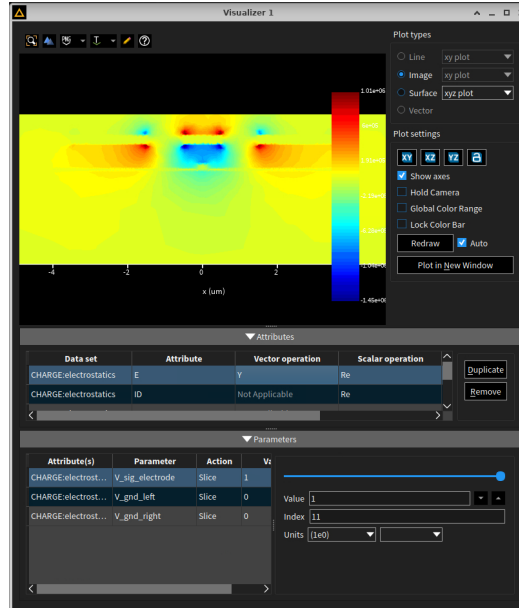


Figure 5.10: CHARGE result:  $E_y(x, y)$  distribution under a single-ended 1 V drive. This component is later mapped to the LN  $c$ -axis field component  $E_c$  according to the adopted crystal-axis mapping and is used to evaluate the EO overlap with the optical TE<sub>0</sub> mode.

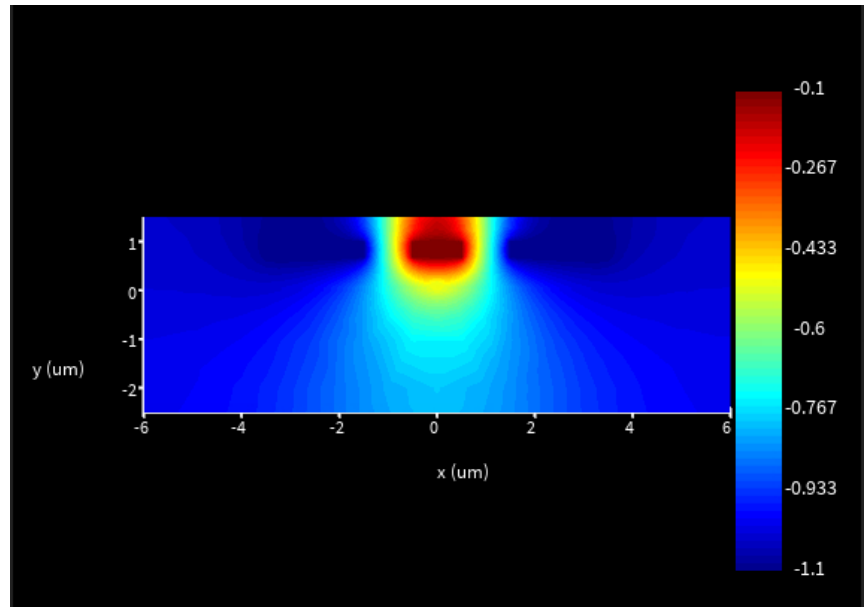


Figure 5.11: CHARGE result: electrostatic potential  $V(x, y)$  for a 1 V single-ended bias. The potential drop is localized around the electrode gap region, validating the applied boundary conditions and the simulation region coverage.

### 5.2.3 $V_\pi L$ evaluation by combining CHARGE and MODE results

This subsection explains how the electrostatic results from CHARGE are combined with the optical eigenmode from MODE to compute the half-wave voltage-length product  $V_\pi L$ . The overall procedure is: (i) save the CHARGE field results at 1 V, (ii) load both the CHARGE dataset and the MODE TE<sub>0</sub> mode fields in MODE, (iii) map the CHARGE field onto the MODE grid, (iv) compute a mode-weighted field overlap, and (v) convert the resulting  $\Delta n_{\text{eff}}/V$  into  $V_\pi L$ .

**Step 1: Saving CHARGE outputs** After running the electrostatic solver, the CHARGE monitor outputs the potential  $V(x, y)$  and in-plane field components  $E_x(x, y)$  and  $E_y(x, y)$  at 1 V. These datasets are exported and stored as a MATLAB .mat file for use in MODE.

**Step 2: Optical mode weight from MODE (TE<sub>0</sub>)** In MODE, the fundamental TE-like eigenmode (TE<sub>0</sub>) is computed and provides the optical-field components on a structured grid  $(x_m, y_m)$ . The optical intensity weight used for overlap integration is defined as

$$W(x, y) = |E_{\text{opt}}(x, y)|^2 = |E_x(x, y)|^2 + |E_y(x, y)|^2 + |E_z(x, y)|^2. \quad (5.24)$$

**Step 3: Mapping CHARGE fields onto the MODE grid** CHARGE exports the electrostatic fields on a scattered-point mesh, whereas MODE fields are defined on a structured grid. To enable pointwise multiplication with  $W(x, y)$ , the CHARGE field samples are mapped onto the MODE grid using a nearest-neighbor correspondence. The mapping index is first constructed on the MODE grid and then reused to obtain  $E_x$  and  $E_y$  on the same grid:

$$k(i, j) = \arg \min_p \left[ (c_x(p) - x_m(i))^2 + (c_y(p) - y_m(j))^2 \right], \quad (5.25)$$

$$E_x^{\text{on}}(i, j) = E_x^{\text{CHARGE}}(k(i, j)), \quad E_y^{\text{on}}(i, j) = E_y^{\text{CHARGE}}(k(i, j)). \quad (5.26)$$

Following the adopted crystal-axis mapping, the driving-field component along the LN *c*-axis is taken as

$$E_c(x, y) = E_y^{\text{on}}(x, y). \quad (5.27)$$

**Step 4: Mode-weighted overlap field** The mode-weighted average driving field is computed as

$$F_c = \langle E_c \rangle_W = \frac{\iint W(x, y) E_c(x, y) dA}{\iint W(x, y) dA}. \quad (5.28)$$

**Step 5:  $\Delta n_{\text{eff}}/V$  and  $V_\pi L$**  Using a linear Pockels approximation, the effective-index change per volt is estimated by

$$\frac{\Delta n_{\text{eff}}}{V} \approx -\frac{1}{2} n^3 r F_c, \quad (5.29)$$

and the half-wave voltage-length product follows:

$$V_\pi L = \frac{\lambda}{2 |\Delta n_{\text{eff}}/V|}. \quad (5.30)$$

**MODE script used for calculation** The following excerpt lists the essential script lines we used in MODE to (i) read the TE<sub>0</sub> modal fields, (ii) load the CHARGE dataset, (iii) perform nearest-neighbor mapping, and (iv) compute  $F_c$ ,  $\Delta n_{\text{eff}}/V$ , and  $V_\pi L$ .

```
#MODE: read TE0 fields and build optical weight W
p = "FDE::data::mode1";
xm = getresult(p,"x"); ym = getresult(p,"y");
Exm = getresult(p,"Ex"); Eym = getresult(p,"Ey"); Ezm = getresult(p,"Ez");
W = pinch(abs(Exm)^2 + abs(Eym)^2 + abs(Ezm)^2);

#Load CHARGE results exported as .mat
matlabload("charge_E_1V.mat");
cx = x; cy = y; cEx = Ex; cEy = Ey; # rename to avoid overwriting xm,ym

#Nearest-neighbor map from CHARGE points to MODE grid
Nx = length(xm); Ny = length(ym);
idx_map = matrix(Nx,Ny);
for (j=1:Ny) { y0=ym(j);
  for (i=1:Nx) { x0=xm(i);
    r2=(cx-x0)^2+(cy-y0)^2; k=find(r2==min(r2));
    idx_map(i,j)=k(1);
  }
}
Ex_on = matrix(Nx,Ny); Ey_on = matrix(Nx,Ny);
```

```

for (j=1:Ny) { for (i=1:Nx) {
    k=idx_map(i,j); Ex_on(i,j)=cEx(k); Ey_on(i,j)=cEy(k);
}}
#c-axis field component and overlap factor
E_c = Ey_on;
dx = xm(2)-xm(1); dy = ym(2)-ym(1); dA = dx*dy;
F_c = (sum(sum(W*E_c))*dA) / (sum(sum(W))*dA);

#Case comparison: (n_o,r13) vs (n_e,r33)
lambda = 0.422e-6;
n_o = 2.4089; n_e = 2.3063;
r13 = 8.6e-12; r33 = 30.8e-12;

dn_o13 = -0.5*n_o^3*r13*F_c; VpiL_o13 = lambda/(2*abs(dn_o13));
dn_e33 = -0.5*n_e^3*r33*F_c; VpiL_e33 = lambda/(2*abs(dn_e33));

```

#### 5.2.4 Final $V_\pi L$ results and comparison

The mode-weighted average driving field along the LN  $c$ -axis is obtained as

$$F_c = \langle E_c \rangle_W \approx -1.47494 \times 10^5 \text{ V/m}. \quad (5.31)$$

With  $\lambda = 0.422 \mu\text{m}$ ,  $n_o = 2.4089$ ,  $n_e = 2.3063$ , and representative clamped EO coefficients ( $r_{13} = 8.6 \text{ pm/V}$ ,  $r_{33} = 30.8 \text{ pm/V}$ ), the computed effective-index changes per volt and the corresponding half-wave voltage-length products are:

$$\text{Case A (ordinary): } (n_o, r_{13}) \Rightarrow \frac{\Delta n_{\text{eff}}}{V} \approx 8.86542 \times 10^{-6}, \quad V_\pi L \approx 2.38004 \text{ V} \cdot \text{cm}, \quad (5.32)$$

$$\text{Case B (extraordinary): } (n_e, r_{33}) \Rightarrow \frac{\Delta n_{\text{eff}}}{V} \approx 2.78639 \times 10^{-5}, \quad V_\pi L \approx 0.757251 \text{ V} \cdot \text{cm}. \quad (5.33)$$

**Comparison and interpretation** The extraordinary-index case yields a substantially smaller  $V_\pi L$ :

$$\frac{V_\pi L(n_o, r_{13})}{V_\pi L(n_e, r_{33})} \approx 3.14299, \quad (5.34)$$

which is consistent with the  $n^3r$  scaling of the Pockels-induced index perturbation under an identical field overlap factor  $F_c$ . In other words, when the same electrode-driven  $c$ -axis field distribution is assumed, the larger EO coefficient  $r_{33}$  leads to a stronger effective-index modulation and therefore a lower  $V_\pi L$ .

# Chapter 6

## Conclusion

This work targeted the design and simulation of an LNOI (x-cut) electro-optic (EO) phase shifter and its integration into a Mach-Zehnder interferometer (MZI) switch. First, the guided optical mode was characterized using *Ansys Lumerical MODE* (FDE), where the fundamental  $TE_0$  mode was identified under the chosen LNOI waveguide stack and geometry. Next, *Lumerical CHARGE* was used to compute the electrode-driven electric-field distribution within the EO region. By mapping the crystal axes and applying the Pockels effect with the material anisotropy, the voltage-phase conversion efficiency was quantified and the key phase-shifter figure of  $V_\pi L$  was extracted.

While the extraction of  $V_\pi L$  validates the EO phase-shifter efficiency at the cross-section level, it does not directly yield the full-switch metrics of interest for an MZI switch (insertion loss, extinction ratio, and crosstalk). Therefore, the next step of this project is to perform circuit-level simulations using *EME* to evaluate the complete MZI transfer behavior. In *EME*, the MZI switch will be modeled as a structure consisting of two directional couplers (DCs) and a central EO phase-shifter section:

$$\text{DC (50:50)} \rightarrow \text{Phase Shifter} \rightarrow \text{DC (50:50)},$$

forming a four-port device (two inputs and two outputs). The input excitation will be the fundamental guided TE mode at the input ports, and the output port transmissions will be computed from the resulting scattering matrix (S-matrix), leading to IL, ER, and XT values.

Beyond simulation, an extension of this study is to fabricate the proposed LNOI MZI switch in a cleanroom environment and validate the predicted performance experimentally.

# Bibliography

- [1] A. Singh, A. Sethia, L. Esmaeilifar, R. Valivarthi, N. Sinclair, M. Spiropulu, and D. Oblak, “Photonic quantum information with time-bins: Principles and applications,” 2025.
- [2] G. A. Reider, *Photonics: An Introduction*. Cham: Springer International Publishing, 2016. eBook ISBN 978-3-319-26076-1.
- [3] B. E. A. Saleh and M. C. Teich, *Fundamentals of Photonics*. Hoboken, NJ: John Wiley & Sons, 3 ed., 2019. Two-volume set.
- [4] D. Sakuma, A. Taherkhani, T. Tsuno, T. Sasaki, H. Shimizu, K. Teramoto, A. Todd, Y. Ueno, M. Hajdušek, R. Ikuta, R. Van Meter, and S. Nagayama, “An optical interconnect for modular quantum computers,” 2024.
- [5] S. Majidy, C. Wilson, and R. Laflamme, *Building Quantum Computers: A Practical Introduction*. Cambridge University Press, 2024.
- [6] R. S. Sutor, *Dancing with Qubits*. Packt Publishing, 2 ed., 2024.
- [7] PsiQuantum team, “A manufacturable platform for photonic quantum computing,” *Nature*, vol. 641, 2025.
- [8] S. Saha, M. Shalaev, J. O'Reilly, I. Goetting, G. Toh, A. Kalakuntla, Y. Yu, and C. Monroe, “High-fidelity remote entanglement of trapped atoms mediated by time-bin photons,” *Nature Communications*, vol. 16, p. 2533, 2025.
- [9] S. Sciara, G. M. Hounsa, N. Montaut, H. Yu, A. Martin, B. Boulanger, T. Chartier, J. Azaña, and R. Morandotti, “Quantum key distribution implemented with d-level time-bin entangled photons,” *Nature Communications*, vol. 16, p. 171, 2025.
- [10] H. Yu, B. Crockett, N. Montaut, S. Sciara, M. Chemnitz, S. T. Chu, B. E. Little, D. J. Moss, Z. Wang, J. Azaña, and R. Morandotti, “Exploiting nonlocal correlations for dispersion-resilient quantum communications,” *Physical Review Letters*, vol. 134, 2025.

- [11] Y. Zheng, H. Zhong, H. Zhang, L. Song, J. Liu, Y. Liang, Z. Liu, J. Chen, J. Zhou, Z. Fang, M. Wang, L. Li, R. Wu, and Y. Cheng, “Electro-optically programmable photonic circuits enabled by wafer-scale integration on thin-film lithium niobate,” *Physical Review Research*, vol. 5, 2023.
- [12] S. Raghunathan, R. Oliver, Y. Zhao, K. McNulty, C. Joshi, M. Lipson, and A. L. Gaeta, “Telecom-to-visible quantum frequency converter on a silicon nitride chip,” 2025.
- [13] T. Maegami, R. Akimoto, K. Fujii, K. Nakazawa, T. Koshida, and M. Kato, “Propagation loss evaluation of sin waveguides for visible light,” 2021. in Japanese.
- [14] F. Vedovato, *Quantum Optics Experiments in Space*. PhD thesis, Università degli Studi di Padova, 2018.
- [15] J. Joo, J. Park, and G. Kim, “Cost-effective 2x2 silicon nitride mach–zehnder interferometric (mzi) thermo-optic switch,” *IEEE Photonics Technology Letters*, vol. 30, no. 8, pp. 740–743, 2018.
- [16] G. B. Xavier, J.-Å. Larsson, P. Villoresi, G. Vallone, and A. Cabello, “Energy-time and time-bin entanglement: past, present and future,” *npj Quantum Information*, vol. 11, p. 129, 2025.
- [17] A. J. Mercante, S. Shi, P. Yao, L. Xie, R. M. Weikle, and D. W. Prather, “Thin film lithium niobate electro-optic modulator with terahertz operating bandwidth,” *Optics Express*, vol. 26, no. 11, pp. 14810–14816, 2018.
- [18] J. Wang, P. Chen, D. Dai, and L. Liu, “Polarization coupling of x-cut thin film lithium niobate based waveguides,” *IEEE Photonics Journal*, vol. 12, no. 3, p. 2200310, 2020.
- [19] D. Zhu, L. Shao, M. Yu, R. Cheng, B. Desiatov, C. J. Xin, Y. Hu, J. Holzgrafe, S. Ghosh, A. Shams-Ansari, E. Puma, N. Sinclair, C. Reimer, M. Zhang, and M. Lončar, “Integrated photonics on thin-film lithium niobate,” *Advances in Optics and Photonics*, vol. 13, no. 2, pp. 242–352, 2021.
- [20] M. Fox, *Quantum Optics: An Introduction*. Oxford University Press, 2006.
- [21] R. Van Meter, *Quantum Networking*. Wiley-ISTE, 2014.
- [22] M. Segev, Y. Silberberg, and D. N. Christodoulides, “Anderson localization of light,” *Nature Photonics*, vol. 7, pp. 197–204, 2013.

- [23] J. M. Donohue, M. Agnew, J. Lavoie, and K. J. Resch, “Coherent ultrafast measurement of time-bin encoded photons,” *Phys. Rev. Lett.*, vol. 111, p. 153602, Oct 2013.
- [24] A. Patil and S. Guha, “Clifford manipulations of stabilizer states: A graphical rule book for Clifford unitaries and measurements on cluster states, and application to photonic quantum computing,” 2023.
- [25] N. Euler, M. Monika, U. Peschel, and M. Gärttner, “Detecting high-dimensional time-bin entanglement in fiber-loop systems,” *Phys. Rev. A*, vol. 112, p. 012410, Jul 2025.
- [26] A. Tchebotareva, S. L. N. Hermans, P. C. Humphreys, D. Voigt, P. J. Harmsma, L. K. Cheng, A. L. Verlaan, N. Dijkhuizen, W. de Jong, A. Dréau, and R. Hanson, “Entanglement between a diamond spin qubit and a photonic time-bin qubit at telecom wavelength,” *Phys. Rev. Lett.*, vol. 123, p. 063601, Aug 2019.
- [27] S. I. Davis, R. Valivarthi, A. Cameron, C. Pena, S. Xie, L. Narvaez, N. Lauk, C. Li, K. Taylor, R. Youssef, C. Wang, K. Kapoor, B. Korzh, N. Sinclair, M. Shaw, P. Spentzouris, and M. Spiropulu, “Entanglement swapping systems toward a quantum internet,” 2025.
- [28] J. Brendel, N. Gisin, W. Tittel, and H. Zbinden, “Pulsed energy-time entangled twin-photon source for quantum communication,” *Phys. Rev. Lett.*, vol. 82, pp. 2594–2597, Mar 1999.
- [29] G. Finco, F. Miserocchi, A. Maeder, *et al.*, “Time-bin entangled Bell state generation and tomography on thin-film lithium niobate,” *npj Quantum Information*, vol. 10, p. 135, 2024.
- [30] M. Avesani *et al.*, “Full daylight quantum-key-distribution at 1550 nm enabled by integrated silicon photonics,” *npj Quantum Information*, vol. 7, pp. 1–8, 2021.
- [31] A. Politi, M. J. Cryan, J. G. Rarity, S. Yu, and J. L. O’Brien, “Silica-on-silicon waveguide quantum circuits,” *Science*, vol. 320, no. 5876, pp. 646–649, 2008.
- [32] N. Gisin and R. Thew, “Quantum communication,” *Nature Photonics*, vol. 1, pp. 165–171, 2007.